2019-01-25

Molecular Ions in Ion Upflows and their Effect on Hot Atomic Oxygen Production

Foss, Victoria

UNIVERSITY OF CALGARY

Molecular Ions in Ion Upflows and their Effect on Hot Atomic Oxygen Production

by

Victoria Foss

A THESIS

SUBMITTED TO THE FACULTY OF GRADUATE STUDIES

IN PARTIAL FULFILMENT OF THE REQUIREMENTS FOR THE

DEGREE OF MASTER OF SCIENCE

GRADUATE PROGRAM IN PHYSICS AND ASTRONOMY

CALGARY, ALBERTA

JANUARY, 2019

Abstract

We present results from the Imaging and Rapid Scanning Mass Spectrometer (IRM) on board the Enhanced Polar Outflow Probe (e-POP), on the occurrence morphology and frequency of molecular ions in the topside ionosphere. Molecular ions are observed at all e-POP altitudes at high latitudes, in much greater abundances than predicted by empirical models of the ionosphere, during both active and quiet times. Large count rate events occur in greater frequency in the pre-midnight sector (20-22 magnetic local time (MLT)). These large count rate events also show a correlation to the main and recovery phases of large geomagnetic storms.

Molecular NO^+ and O_2^+ ions can undergo dissociative recombination with electrons to produce non-thermal oxygen atoms, which disturb the local equilibrium and increase satellite drag in low Earth orbit (LEO). We simulate this production with the linearized Boltzmann equation using both the International Reference Ionosphere (IRI) and augmented models based on IRM observations. It is found that NO^+ concentrations of 10% result in an apparent hot temperature of 0.19 eV, or 0.3 eV in the case of O_2^+. We discuss the significance of these results as well as their implications on magnetosphere-ionosphere-thermosphere (MIT) coupling.

Acknowledgements

This thesis would not have been possible without the help of numerous individuals. First and foremost, I would like to thank my supervisor, Andrew Yau, for his patience, enthusiasm, guidance and immense knowledge. It has truly been an honor to learn and grow under his leadership.

Thanks are also due to the e-POP Science Team who fielded my numerous (and often trivial) questions, guided me in coding and data interpretation, and supported my research in any way they could manage. I am particularly grateful for their regular supply of coffee and overall comradery. Andrew H., Andrew W., Greg, Troy, Jamie, it has been a pleasure to work with you all, thank you for making me feel so welcome and supported.

A big thanks to Dr. Bernie Shizgal and Dr. Konstantin Kabin who produced the Boltzmann equation simulation which I modified for part of my analysis.

Lastly, a huge thank you to my husband, Sean. His endless support and encouragement during the hardest points helped me keep things in perspective and keep pushing on. He kept a handle on things at home, so I could put in long hours at the office, and supported me in every way he could manage. He is my biggest cheerleader, my best friend, and I absolutely could not have done this without him.

Contents

List of Tables

List of Figures

List of Symbols, Abbreviations & Nomenclature

Acronym	**Definition**
AE	Auroral Electrojet
AL	Auroral Lower
AU	Auroral Upper
CASSIOPE	Cascade Smallsat and Ionospheric Polar Explorer
DE-1	Dynamic Explorer 1
Dst	Disturbance Storm Time
e-POP	Enhanced Polar Outflow Probe
EUV	Extreme Ultraviolet
F10.7	10.7 cm Flux
FLIP	Field Line Interhemispheric Plasma
FWHM	Full width half maximum
HEA	Hemispherical Electrostatic Analyzer
IRI	International Reference Ionosphere
IRM	Imaging and Rapid Scanning Mass Spectrometer
Kp	Planetary K-index
LEO	Low Earth Orbit
MCP	Micro-channel Plate
MIT	Magnetosphere Ionosphere Thermosphere
MLT	Magnetic Local Time
MSIS	Mass Spectrometer Incoherent Scatter

SFU	Solar Flux Unit
TEC	Total Electron Content
TIEGCM	Thermosphere Ionosphere Electrodynamics General Circulation Model
TOA	Time of Arrival
TOF	Time of Flight
UV	Ultraviolet
Symbol	**Definition**
g	Acceleration due to gravity
G	Gravitational Force
$J(f)$	Collision Operator
k_B	Boltzmann constant
m	Mass
M_E	Mass of the Earth
n	Number density
nT	Nanotesla
q	Atomic charge
$S(v)$	Source velocity distribution
$\vec{r}$	Position vector relative to center of Earth
R_E	Earth Radius
T	Temperature
$\vec{v}$	Velocity
z	Altitude (geoid)

1 Introduction

1.1 Research Objectives

The present research is comprised of a statistical analysis of ion composition data from the e-POP (Enhanced Polar Outflow Probe) Imaging and Rapid-Scanning Mass Spectrometer (IRM) which investigates the occurrence morphology of molecular ions in the high-latitude ionosphere, and a theoretical simulation study to examine the possible effects of the observed molecular ions on hot atomic oxygen production.

The presence of a geocorona of energetic atomic oxygen in the terrestrial upper atmosphere (thermosphere) has been the subject of many scientific investigations in recent decades. The presence was theoretically predicted (Rohrbaugh & Nisbet, 1973), and subsequently observed from optical measurements of the high-altitude airglow (Yee, Meriwether, & Hays, 1980; Cotton, Gladstone, & Chakrabarti, 1993). A geocorona is formed through various chemical processes and contains atoms with non-thermal kinetic energy (up to a few electron volts), which is a source of heating in the upper atmosphere (Whipple, 1974; Yee, 1988). Studies have suggested that this energetic population of atomic oxygen has certain effects on satellites in Low Earth Orbit (LEO), particularly during strong solar storms (Shematovich et al., 2011).

The dissociative recombination of molecular ion species such as NO^+ and O_2^+ has been proposed as a significant source of these hot atoms, though additional processes such as charge exchange and collisional quenching have also been considered, particularly in the lower thermosphere (Rohrbaugh & Nisbet, 1973; Richards, Hickey, & Torr, 1994; Hickey, Richards, & Torr, 1995).

This study uses data from the IRM instrument on the Enhanced Polar Outflow Probe (e-POP), which has a unique capability to distinguish molecular ions from other (atomic) species (Yau &

Howarth, 2016) and simultaneously resolve their incident energies and directions in the topside ionosphere. IRM data spanning a 4-year period (from January 2014 to December 2017) were analyzed to identify the times, locations and abundances of molecular ions observed at all e-POP altitudes, to estimate their occurrence frequency and abundance distributions as well as their possible correlations with solar and geomagnetic activity levels.

A simulation was performed to estimate the effects of dissociative recombination of the observed molecular ions on the atomic oxygen energy distribution. A linearized Boltzmann equation was employed in conjunction with thermospheric and ionospheric attitude profiles to solve for the atomic oxygen velocity (or the equivalent energy) distribution resulting from the dissociative recombination and subsequent collisional relaxation. Using the empirical International Reference Ionosphere (IRI) model (e.g. Bilitza 2001) and augmented models based on the e-POP observations, respectively, the resulting overall atomic oxygen energy distribution was determined as a function of altitude in each case, and the corresponding hot oxygen temperature was compared with previous predictions and measurements.

1.2 Earth's Thermosphere and Ionosphere

The Earth's dayside atmosphere is constantly illuminated by electromagnetic radiation from the Sun. The photons in the extreme ultraviolet (EUV) and ultraviolet (UV) portion of the solar spectrum have sufficient energy to dissociate both molecular oxygen and nitrogen (photodissociation), producing atomic oxygen and nitrogen in the upper atmosphere (thermosphere), and to ionize both the resulting atoms and the (original) molecules (photoionization, including dissociative photoionization in the latter case), forming our ionosphere. The ionosphere contains three distinct regions, the D, E, and F layers (or regions), with the F region sometimes separating into what are known as the F_1 and F_2 regions. These regions are shown schematically in Figure 1.1, and each is characterized by an electron density maximum at a certain altitude.

The D region spans the region of about 70 to 90 km altitude; it is more weakly ionized (compared with the E and F regions), and is dominated by both positive and negative molecular ions. The E region, which extends from about 90 to 150 km altitude, is dominated by (positive) molecular ions. In this region, chemical time constants are short enough that plasma transport processes can largely be neglected, and the region is governed primarily by photochemistry (Schunk & Nagy, 2009).

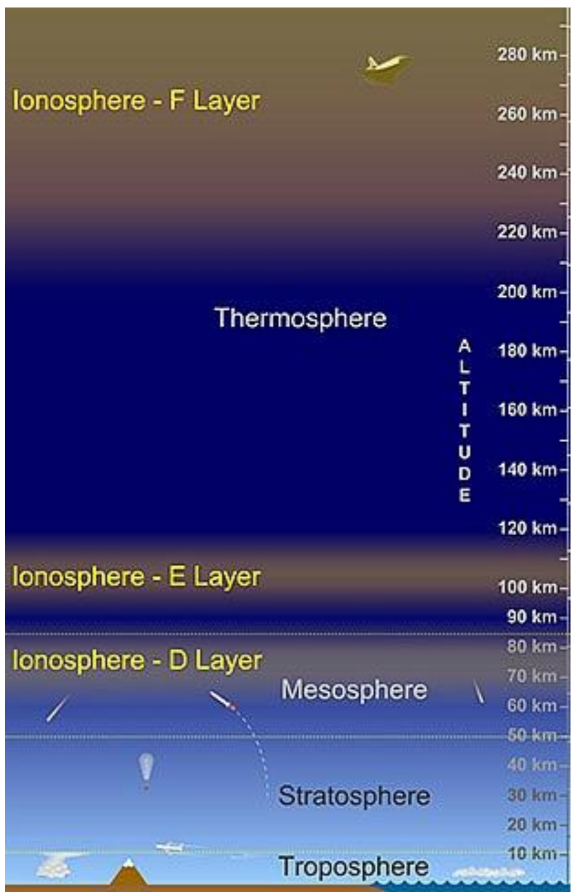

Figure 1.1: Layers of the thermosphere and ionosphere. This figure demonstrates the vertical structure and approximate locations of key regions of the thermosphere and embedded ionosphere. Image courtesy of the UCAR Center for Science Education.

The F region, the uppermost region, contains two local peaks, F_1 and F_2. This region, which extends from ~150 km to the exobase (~400 km near solar minimum to ~550 km near solar maximum), is dominated by atomic species, specifically O and O^+, and governed primarily by transport processes and by collisions between the charged particles and the neutrals. With a substantial neutral density, collisions between charged particles and neutrals must be considered.

The ionosphere varies greatly due to changes in the source of ionization as well as changes in the thermosphere. In response to periodic solar EUV/UV radiation, the ionosphere varies predictably within each 24-hour period, as well as with the 11-year solar cycle (and within a 27-day solar rotation period near solar maximum). In the presence of photoionization in the daytime ionosphere, more ions are created than are destroyed in the middle of the day. Conversely, at night recombination processes dominate, with the D region generally disappearing entirely and the F region collapsing to a single peak. The E region generally disappears at mid to low latitudes but can be present in polar regions due to the precipitation of energetic auroral electrons.

Another driving force in the ionosphere is the neutral atmosphere, in which it exists. Thermospheric winds can push ions along magnetic field lines to different altitudes, and changes in the local neutral composition can affect ion production and recombination rates (Meriwether, Biondi, & Anderson, 1985). The different ionospheric regions are affected to different extents by geomagnetic and solar activity, and as a result the field of magnetosphere-ionosphere-thermosphere coupling has been of great scientific interest in recent decades.

1.2.1 MSIS-E Model

The densities within the neutral atmosphere are governed by a balance of the vertical gravitational force and the thermal-pressure gradient force. In the upper atmosphere, where diffusion dominates over molecular mixing, the density of a given species is given by the barometric pressure law:

$$n(z) = n(z_0)\exp\left[-\frac{z - z_0}{H}\right] \ ; \qquad H = \frac{k_B T}{mg} \qquad [1.1]$$

where $n(z)$ is the density at altitude z, and n_0 the density at altitude z_0. H is also known as the scale height of a given species, where k_B is the Boltzmann constant, T the temperature, m the particle mass and g acceleration due to gravity (Schunk & Nagy, 2009). It is possible to model the neutral atmosphere using equation [3.1], though much of the dynamics are not captured.

For this reason, empirical models of the thermosphere are a key tool for atmospheric research and modeling. The most commonly used ones are the different versions of the Mass Spectrometer and Incoherent Scatter Radar (MSIS) model. The different MSIS models consist of parametric analytic approximations of the vertical structure of the atmosphere as a function of location, time, solar activity and geomagnetic activity, and provide altitude profiles of temperature, number density of various species (He, O, N_2, O_2, Ar, H, N), total mass density, as well as the number density of “anomalous” or “hot” oxygen in the case of the extended versions of the model; see for example Picone et al., (2002); Yau, Peterson, & Abe, (2011). Figure 1.2 is reproduced from Figure 2 in Yau, Peterson, & Abe (2011), and compares the typical high-latitude density and temperature profiles near solar maximum and minimum, respectively.

The most recent of the MSIS models is the NRLMSISE-00, the successor to the MSISE-90 model, and the model of choice for this research. The model database includes ground, rocket and satellite-based measurements collected over more than two decades. It was expanded to include data from

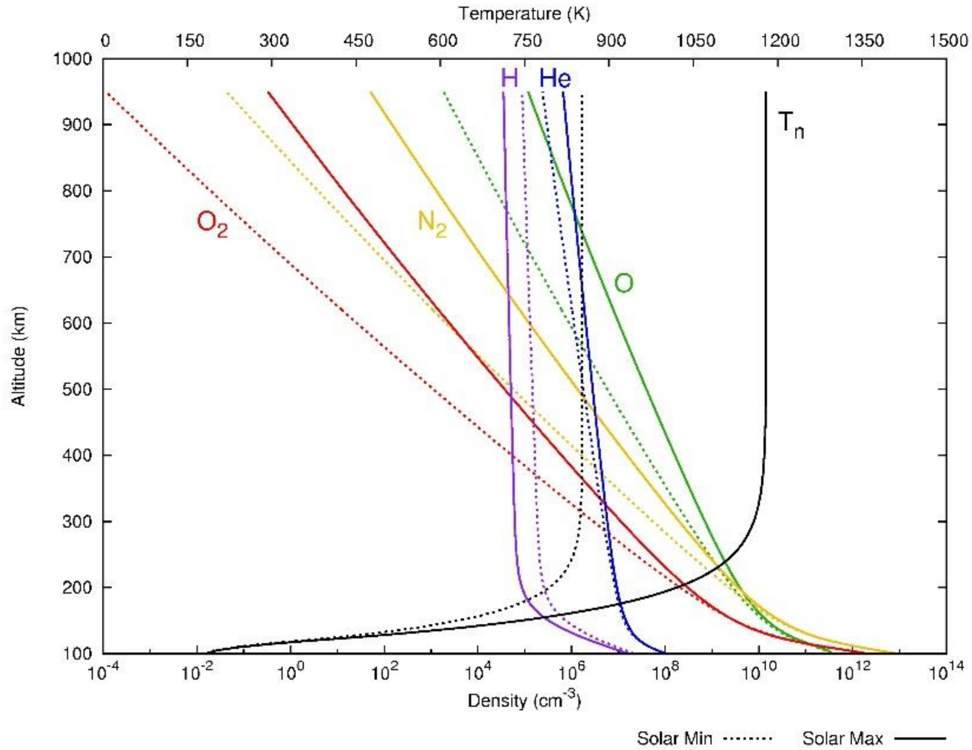

Figure 1.2: Neutral atmospheric density and temperature profiles. Typical high-latitude density and temperature profiles according to the MSIS E-00 model, for solar maximum and solar minimum. Note that atomic oxygen dominates our region of interest for this study.

other neutral atmospheric models, such as the Jacchia model (J77), which estimates parameters such as pressure, temperature and density from satellite drag data. This model is sensitive to geomagnetic activity levels and can provide estimates of the average atmospheric state under storm conditions (Bilitza & Reinisch, 2008). However, at high latitudes and high geomagnetic activity, where data sampling is sparse, the model is not able to specify the density and temperature structures associated with any particular storm.

1.2.2 IRI Model

The International Reference Ionosphere (IRI) model was first developed in the sixties to serve as an empirical standard model of the “standard” ionosphere. It is based on many ground and space observations, so there is little dependence on a still-developing theoretical understanding. The data for the model come from ionosondes, incoherent scatter radars, topside sounders, satellites and sounding rockets from across the globe. For any given location, date, and time, the IRI model predicts the average electron density, electron temperature, ion temperature, ion composition, and Total Electron Content (TEC) (Bilitza, 2001). As with the MSIS-class models, there is a strong dependence on the availability of data, and in some regions the model proves to be less reliable, specifically at high latitudes.

Several theoretical (physics-based) ionospheric models exist, each with unique strengths and weaknesses. The most comprehensive of these models is the Thermosphere Ionosphere Electrodynamics General Circulation Model (TIEGCM), which uses three-dimensional momentum, energy and continuity equations to determine ion and neutral properties at a given time (Roble et al., 1988). The Field Line Interhemispheric Plasma (FLIP) model on the other hand applies to low and mid-latitudes. The implementation of these models can be time consuming and neither necessarily gives more realistic models of molecular ion densities compared with the IRI model, so we chose the latter for this study.

1.3 Solar and Geomagnetic Activity

1.3.1 Solar F10.7 Index

The level of solar activity at a given time is commonly characterized by the F10.7 index, often referred to as the F10.7 flux, an index of the measured solar radio flux at the 10.7 cm wavelength. The daily value of this flux is measured at local noon at the Penticton Radio Observatory in British Columbia. This value has been measured consistently since 1947, making it one of the longest running records of solar activity. It is closely correlated to both the sunspot number and the solar EUV flux, and it can be measured reliably and accurately from the ground in all weather conditions (Tapping, 2013). Figure 1.3 shows the mean, maximum and minimum solar radio flux in each 27-day solar rotation period from 1965 to 2005, or solar cycles 20 to 23. The 10 to 13-year solar activity cycle is apparent. F10.7 index values are given in solar flux units (sfu) where $1\ \text{sfu} = 10^{-22}\,\text{Wm}^{-2}\text{Hz}^{-1}$.

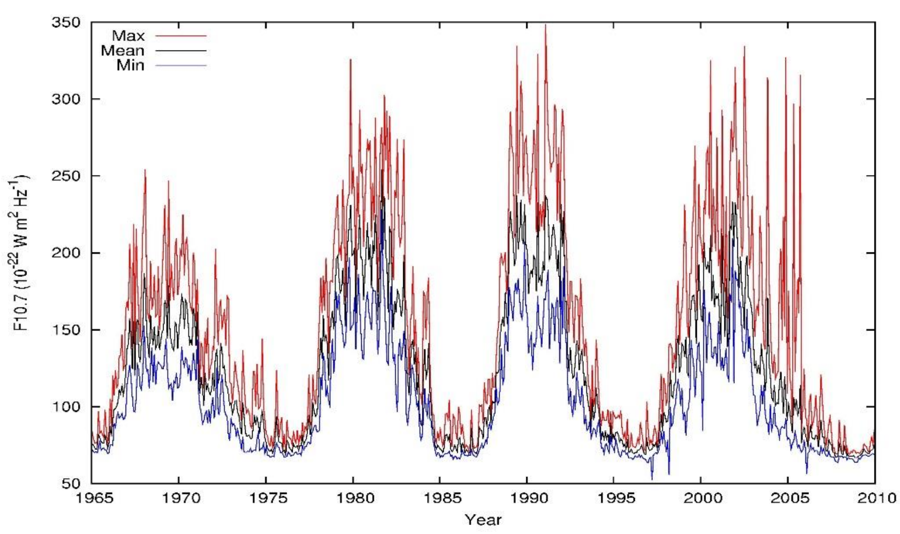

Figure 1.3: Solar F10.7 flux trends. The mean, maximum and minimum solar F10.7 flux for each 27-day solar rotation between 1965 and 2010.

1.3.2 Geomagnetic Activity Indices

1.3.2.1 Dst

The disturbance storm time (Dst) index measures variations in the globally symmetric, westward flowing ring current, a current region which encircles the Earth close to the magnetic equator at geocentric distances of ~2 to ~9 earth radii (R_E). A magnetic storm generally has three phases: the initial, main, and recovery phases. The initial phase is the result of compression of the dayside magnetosphere due to the arrival of a sudden enhancement of the solar wind. The magnetospheric response is characterized by a sudden global increase in the horizontal component of the magnetic field in response to this disturbance, referred to as the sudden storm commencement (SSC). Following the SSC, the horizontal (H) component will remain elevated along with the Dst index for about 2-8 hours, known as the initial phase of the storm (Schunk & Nagy, 2009).

After the initial phase, a global decrease in H begins, indicating the main phase of the storm. The strength of a storm is characterized by the severity of this decrease (Saroso, Iyemori, & Suguira, 1993). The onset of these storms is generally associated with a southward pointing interplanetary magnetic field, which allows for coupling of the solar wind and the magnetosphere through magnetic reconnection.

Dst values are calculated in 1-hour time intervals from data collected at 4 low-latitude monitoring stations that are sufficiently far from the auroral and equatorial electrojets to minimize contributions from mid and auroral latitude magnetic disturbances. The primary strength of the Dst index is its ability to detect all magnetic storms, and to determine the time of onset and recovery, to within one hour. It does not capture the presence of individual substorms (Rostoker, 1972).

1.3.2.2 AE

The Auroral Electrojet Index, or AE Index, gives a global, quantitative measure of magnetic substorm activity within the auroral zone produced from currents flowing within and below the auroral oval and, by proxy, the state of the auroral ionosphere. Data are collected from 12 sub auroral observatories, which provide measures of the maximum eastward and westward electrojet currents every hour. Upper and lower envelopes are drawn to encompass all the data, named AU and AL respectively. The AE index at a given time is then the separation between the upper and lower envelope, such that $AE = AU - AL$.

As with every other geomagnetic activity index, the AE index has both strengths and weaknesses. It is commonly used in the quantitative and qualitative study of substorm morphology, though there is some debate over the true physical interpretation of the summation of the upper and lower envelopes, with some suggesting that AU and AL be used as independent indices (Rostoker, 1972). The primary strength of the AE index is its time resolution, as it is calculated every hour for general use but is also available in shorter (2.5-minute) increments through the World Data Center.

1.3.2.3 Kp

The final index to discuss is the Kp index, which quantifies disturbances in horizontal magnetic field components in three-hour time intervals using a statistical composite of 13 sub-auroral observatories distributed between 44 and 60 degrees north or south geomagnetic latitude (Bartels, Heck, & Johnston, 1939). This disturbance is then converted into a local K index and assigned a value from 0 to 9 on a quasi-logarithmic scale. The Kp index is derived from these values, by calculating a weighted average of all observatory observations.

It has been noted that some of the major shortfalls of the Kp index are due to observatory locations. The stations are at mid latitudes, which prevents interference with the auroral electrojet. It has been well established that the auroral oval expands equatorward during magnetic storm activity, so during times of strong magnetic storms, the Kp index is not necessarily an accurate indicator of the intensity of a substorm, as the electrojet can extend equatorward of the observatories. It is however useful for analyzing long periods of magnetic activity and long-term trends.

1.4 Organization of Thesis

The content of this thesis is divided into two distinct yet related parts, as is the structure. Each chapter will discuss the topic in the context of molecular ions followed by hot atomic oxygen.

In Chapter 2 we first present a brief literature review of the occurrence of both molecular ions and hot oxygen atoms within the ionosphere and thermosphere, respectively. In Chapter 3 we discuss the methodology of research, beginning with the operation of the e-POP (Enhanced Polar Outflow Probe) Imaging and Rapid-Scanning Mass Spectrometer (IRM) instrument and its measurement data, and the identification of molecular ions and the statistical survey of their occurrences. We then discuss the computer simulation code that was developed to solve the Boltzmann equation and quantify the production of the hot atomic oxygen, as well as all the underlying assumptions.

In Chapter 4 we discuss the results of the statistical survey in terms of the occurrence morphology and abundances of molecular ions and their dependences on various geophysical parameters such as magnetic local time (MLT) and the Dst and AE indices. The simulation results are also presented and discussed, in terms of the hot oxygen velocity phase space density distributions and resulting temperatures. Finally, in Chapter 5 we discuss the scientific significance of the results in Chapter

4 and their implications on magnetosphere-ionosphere-thermosphere coupling, and we outline the future directions of our research.

2 Molecular Ions and Hot Atomic Oxygen

In this Chapter, we present a brief literature review of molecular ions in the F-region and topside ionosphere and hot atomic oxygen in the thermosphere.

2.1 Molecular Ions

The ionosphere is formed by the ionization of the neutral atmosphere due to the incident solar radiation. A balance is reached in the steady-state between the ions and neutrals, and between their respective production and loss, resulting in the many neutral and ion density and temperature profiles which vary with solar and geomagnetic activity levels.

Due to the photodissociation of molecular oxygen and nitrogen (cf. Chapter 1) and the resulting dominance of atomic oxygen above the E-region (cf. Chapter 1, Figure 1.2), the F-region ionosphere is generally dominated by atomic oxygen ions (O^+). Consequently, empirical models of the ionosphere predict the presence of very few molecular ions above about 300 km (<1% in IRI, for example), as demonstrated in Figure 2.1 Despite this, there have been a few measurements of molecular ions at much higher altitudes above the F-region. The Isis 2 satellite detected molecular ions at concentrations of 10^3 cm^{-3} at 1400 km altitude, where their expected concentrations are on the order of 1 ion cm^{-3} (Hoffman et al., 1974). This measurement was in a highly disturbed, storm time (Kp=9) and was accompanied by a strong enhancement of the N^+ density. The Active Magnetospheric Particle Tracer Explorers spacecraft, Ion Release Module

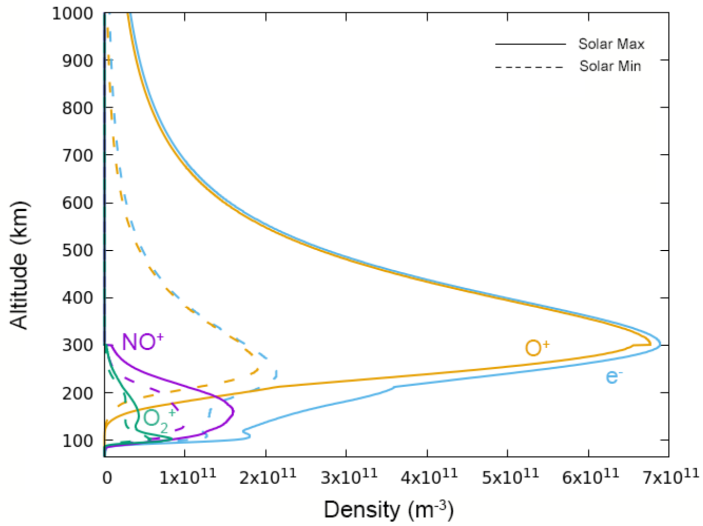

Figure 2.1: Ion and electron density profiles. Mid-latitude summer (45°, June) density profiles of electrons, molecular ions, and O^+ ions according to the IRI model. Results are shown for both solar maximum (solid lines) and solar minimum (dashed lines). Molecular ions appear only in negligible amounts (<1%) above 300 km altitude, regardless of storm conditions.

(AMPTE/IRM) measured energetic (>10's of keV) molecular ions of ionospheric origin, O_2^+ and NO^+ specifically, within the ring current during storm time (Klecker et al., 1986). The Dynamics Explorer 1 (DE-1) detected molecular ions (<50 eV) between 1.0-3.0 R_E geocentric altitude, again during a large magnetic storm (Craven et al., 1985). The OGO-6 spacecraft detected molecular ions at densities exceeding 10^3 ions cm^{-3}, at 1000 km altitude at mid and high latitudes during a relatively undisturbed time (Taylor, 1974), in contrast to the other, disturbed-time measurements above.

More recently, molecular upflowing ions were repeatedly detected on Akebono, again during times of geomagnetic activity (Kp>4). They were seen rarely (3%) and generally in abundances of less than 5%, though occasionally up to 15% (Yau et al., 1993). It has been demonstrated that these molecular ions must be of ionospheric origin, from the F-region in particular (Peterson et al., 1994).

Despite model predictions to the contrary, the experimental evidences on DE-1 and Akebono reveal that molecular ions occur at higher altitude, particularly during storm times. Furthermore, these molecular ions appear to originate as a component of ion upflows, suggesting possible energization processes that could allow them to reach the inner magnetosphere and the ring currents, where they have been previously observed on AMPTE/IRM.

2.2 Hot Atomic Oxygen

Dissociative recombination was first proposed to be an important reaction within the upper atmosphere shortly after the advent of quantum mechanics. In his 1937 paper, H. S. W. Massey sought to use what was previously known about chemical reactions combined with the newfound quantum mechanical knowledge to explain the stratification of atmospheric layers and the daytime variation of the E and F regions of the ionosphere at a qualitative level (Massey, 1937).

Massey noted that if a molecular oxygen ion were to recombine with an electron, it would create an excited, unstable molecule. The dissociation energy of O_2, for example, is less than its ionization energy, so the molecule will spontaneously dissociate into two oxygen atoms. During dissociation the internal binding energy of the molecule is converted into kinetic energy of the resulting atoms, producing atoms with kinetic energy above the average thermal energy of the ambient gas; i.e. $\mathrm{O_2}^{+} + e^{-} \rightarrow \mathrm{O} + \mathrm{O} + \Delta\mathrm{E}$.

Early evidence of this phenomenon in the atmosphere was presented by Hernandez (1971), who observed the atmospheric nightglow with a spectrometer. The first theoretical model of the production of hot atomic oxygen was proposed by Rohrbaugh & Nisbet (1973), in which they demonstrated quantitatively that the dissociative recombination of both NO^+ and O_2^+ could produce hot oxygen atoms with enough energy to disturb the diffusion equilibrium in the upper thermosphere. Yee et. al (1980) provided further experimental evidence of hot oxygen: these authors examined twilight emissions with an interferometer and detected a measurable departure from theoretical predictions, which they attributed to hot oxygen atoms produced through dissociative recombination that were partially thermalized to a temperature of 4000 K or 0.4 eV, and present in concentrations of 10^5-10^6 cm^{-3} above 550 km altitude, as can be seen in Figure 2.2 (Yee, Meriwether, & Hays, 1980). This result was further supported by Hedin (1989), who compared the empirical MSIS-86 model with the Jacchia J70 model, which is an atmospheric

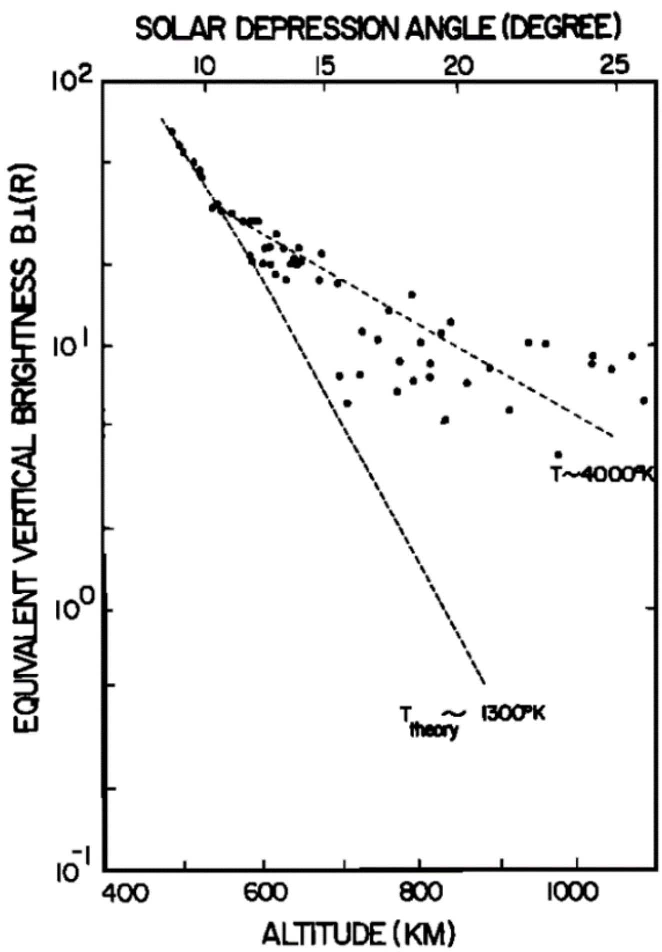

Figure 2.2: Enhanced emissions by Yee, Meriwether, & Hays, (1980). Results highlight an enhancement of emissions at high solar depression angles during quiet solar time. Yee concluded the enhanced emissions suggested the presence of a non-thermal corona of oxygen atoms, with an equivalent temperature of 4000-5000 K.

model based on satellite drag measurements. Hedin attributed the difference between the two models to anomalous drag due to the presence of hot atomic oxygen. In conjunction with Dynamics Explorer 2 mass spectrometer data, he predicted densities of hot oxygen from 1-3×10^4 cm^{-3} at 1100 km during low to moderate solar activity. A sounding rocket observation by Cotton, Gladstone, & Chakrabarti (1993) further supported this result, suggesting a hot oxygen corona with a density of 10^6 cm^{-3} at 550 km and a temperature of 4000 K could be responsible for the enhanced spectroscopic emissions.

A number of different production mechanisms beyond dissociative recombination were considered in the literature and assessed in terms of the resulting impact on the heating of the upper atmosphere. Momentum transfer from energetic O^+ ion precipitation was proposed as a dominant production mechanism over other chemical production mechanisms in quiet daytime conditions (Bisikalo, Shematovich, & Gerard, 1995). The quenching of metastable species and charge exchange have also been considered as significant sources (Whipple, 1974; Shematovich & Bisikalo, 2005; Richards, Hickey, & Torr, 1994). Finally, the influence of these hot oxygen atoms on satellite drag was assessed, and found to be significant above 500 km during strong solar events (Shematovich et al., 2011).

When a molecule undergoes dissociative recombination in which the product atoms are energetically accessible to multiple electronic states, the amount of kinetic energy of the resulting atoms depends upon their final quantum states. The statistical distribution of these final states is given by branching ratios, where the sum of all the ratios is one.

In our analysis we utilize the branching ratios for O_2^+ recombination found by Kella et al. (1997), and the ratios for NO^+ recombination reported in Vejby-Christensen et al. (1998). The branching ratios and exothermicities for both processes are given in Table 2.1.

Table 2.1: Branching ratios and exothermicities of O_2^+ and NO^+ recombination. O_2^+ ratios were obtained from work by Kella et al. (1997), while the NO^+ ratios come from work by Vejby-Christensen et al. (1998). For the purpose of this study, R4 and R7 were omitted due to their low probability of occurrence.

Number	**Reaction**	**Branching Ratio**	$\Delta E_{total}(eV)$	$\Delta E_{oxygen}(eV)$
R1	$O_2^+ + e^- \rightarrow O\left({}^3P\right) + O\left({}^3P\right)$	0.22	6.95	3.48
R2	$O_2^+ + e^- \rightarrow O\left({}^3P\right) + O\left({}^1D\right)$	0.42	4.99	2.50
R3	$O_2^+ + e^- \rightarrow O\left({}^1D\right) + O\left({}^1D\right)$	0.31	3.02	1.51
R4	$O_2^+ + e^- \rightarrow O\left({}^3P\right) + O\left({}^1S\right)$	<0.01	2.77	1.29
R5	$O_2^+ + e^- \rightarrow O\left({}^1D\right) + O\left({}^1S\right)$	0.5	0.80	0.40
R6	$NO^+ + e^- \rightarrow N\left({}^4S\right) + O\left({}^3P\right)$	0.22	2.77	1.28
R7	$NO^+ + e^- \rightarrow N\left({}^4S\right) + O\left({}^1D\right)$	<0.01	0.80	0.37
R8	$NO^+ + e^- \rightarrow N\left({}^2D\right) + O\left({}^3P\right)$	0.78	0.38	0.18

3 Methodology

In this Chapter, we first discuss the e-POP IRM data set, data products, and analysis methods for determining molecular ion occurrence morphology (Section 3.1). We then detail the method developed to simulate the production of hot oxygen atoms via the dissociative recombination of molecular ions (Section 3.2).

3.1 Molecular Ion Occurrence Morphology

3.1.1 The Enhanced Polar Outflow Probe (e-POP)

The Enhanced Polar Outflow Probe (e-POP) is a payload suite of 8 scientific instruments on board the polar-orbiting CASSIOPE small satellite. e-POP was designed to study plasma processes in the high-latitude ionosphere, specifically plasma outflow and related auroral acceleration and radio wave processes (Yau & James, 2015). The e-POP instruments are listed in Table 3.1, and are chosen to measure ion outflow and associated neutral, and radio processes at high resolution.

Table 3.1: The Enhanced Polar Outflow Probe instrument suite.

Instrument Acronym	Instrument Name	Measurement / Data
CER	Coherent EM Radio Tomography	Total Electron Content
FAI	Fast Auroral Imager	Infrared and visible auroral images
GAP	GPS Attitude and Profiling Experiment	Spacecraft position and attitude; plasma density profile (by radio occultation)
IRM	Imaging and Rapid-Scanning Mass Spectrometer	Low energy ion composition and velocity
MGF	Fluxgate Magnetometer	3-D magnetic field; inferred field-aligned currents
NMS	Neutral Mass Spectrometer	Neutral particle mass and velocity
RRI	Radio Receiver Instrument	Radio waves (VLF and HF)
SEI	Suprathermal Electron Imager	Low energy ion and electron 2D energy distributions

3.1.2 Imaging and Rapid Scanning Mass Spectrometer (IRM)

Of primary interest to this study is the Imaging and Rapid-Scanning Ion Mass Spectrometer (IRM), a device capable of measuring the composition and velocity distributions of thermal-energy ions. The IRM on e-POP is designed to measure the ion mass composition and velocity distributions of plasma in the F-region and topside ionosphere, by measuring the energy per charge, azimuth and time of arrival of each detected ion. It uses a hemispherical electrostatic analyzer (HEA) in conjunction with a time of flight (TOF) gate, and a set of toroidal electrostatic deflectors (which are used only when IRM is in its special operation mode; Yau & Howarth, 2016). Figure 3.1(a) depicts the operation of the HEA in an IRM measurement. The IRM sensor is mounted on a 1 m boom with its axis of symmetry along the –Y axis of the CASSIOPE spacecraft. This gives the sensor's planar aperture a 360° view in the X-Z spacecraft plane: with the spacecraft in its nominal, nadir-pointing mode, the Z-axis points toward the nadir, and the X-axis is oriented in the spacecraft velocity (ram) direction. The HEA consists of a pair of hemispherical electrodes ("domes"). In an IRM measurement, the inner dome is biased at a fixed, negative potential (bias voltage) V_{SA} with

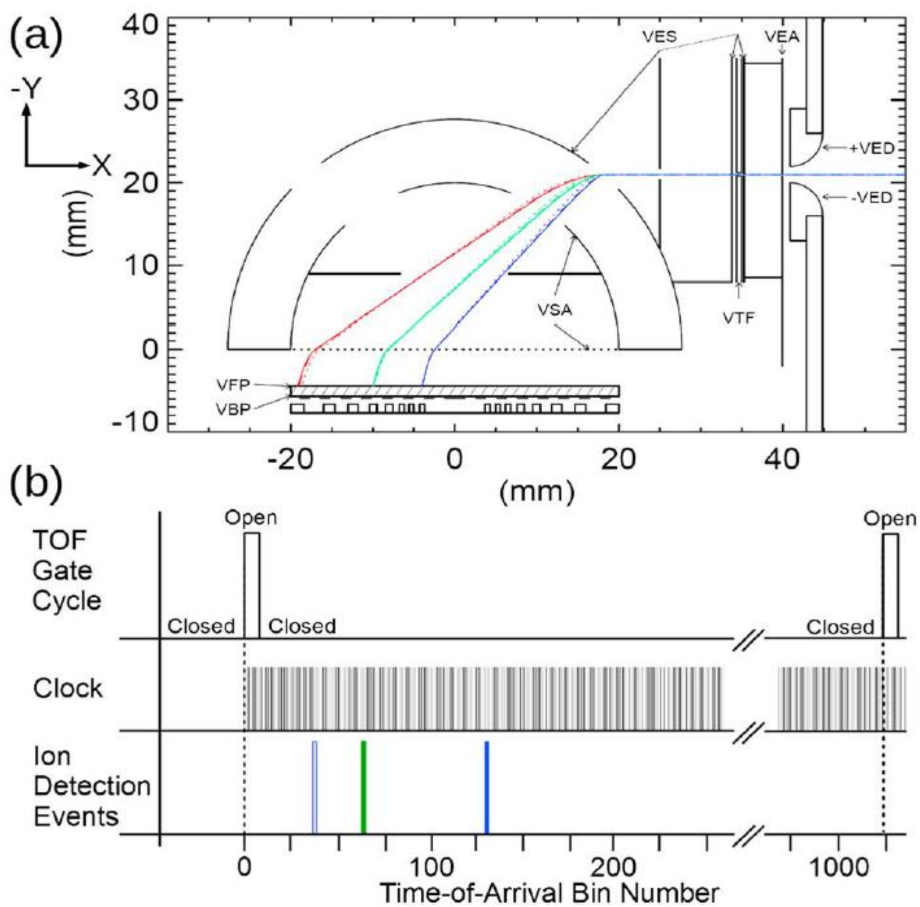

Figure 3.1: IRM instrument design and TOF gate. Presented in panel (a) is a schematic cross section of the IRM sensor as well as simulated ion trajectories for ions with E/q values of 1.3 (blue), 12.5 (green) and 45.0 (red) eV/q, respectively. Panel (b) shows the time-of-flight gate operation and the TOF cycle. Ions of the same energy (1.3 eV/q; blue) but different masses (1 AMU/e, blue open; 16 AMU/e, blue solid) arrive at much different times.

respect to the outer dome. The electric field between the two domes disperses the incident ions by their energy per charge (E/q) ratio and azimuth onto a microchannel plate (MCP) detector.

The MCP detector contains 64 discrete detector pixels, arranged into 8 logarithmically-spaced "energy" sectors radially, and 8 equally-spaced azimuth sectors azimuthally. The traces in Figure 3.1(a) show the simulated trajectory and dispersion of "spacecraft ram" ions with 1.3, 12.5 and 45.0 eV/q inside the sensor for a particular bias voltage. Note that these ions are from the spacecraft ram direction (+X axis) and each of these ions lands on a different detector pixel in the anti-ram sector (i.e. along the –X-axis); it can be seen that ions from the zenith direction above the sensor (–Z-axis) would land on detector pixels in the nadir-pointing sector (+Z-axis), which is into the page in this figure.

Figure 3.1(b) shows the operation of the TOF gate, and illustrates the time of arrival signal that is registered by the TOF gate timing circuitry at the instant of ion detection. A single TOF cycle of IRM consists of 1024 time bins at 40 ns each, so each single TOF cycle is 40.96 μs in length. In an IRM measurement, the TOF gate opens and closes repeatedly, controlled by a pair of fast-switching electrodes, and the TOF cycle is repeated 240-400 times in a typical measurement. This figure shows the simulated arrival of a 1.3 eV H^+ ion (blue, open), before that of an O^+ ion of identical energy (blue solid) and an O^+ ion with greater (12.5 eV) energy (green solid), respectively. While the TOF gate does not measure the ion time of flight (TOF) directly, it is possible to estimate the TOF, within a range, based on the ion time of arrival (TOA). The minimum ion TOF ($TOF_{\min}$) coincides with the minimum ion TOA ($TOA_{\min}$), $TOF_{MIN} = TOA_{MIN}$, and corresponds to a detected ion which arrived at the TOF gate immediately upon gate opening. The maximum possible ion TOF is $TOF_{MAX} = TOA_{MAX} - TOF_{GATE}$, where TOF_{GATE} is the duration of the gate-open period; TOA_{max} is the maximum ion TOA, and corresponds to a detected ion that entered the gate at the last possible moment before TOF gate closing.

When IRM is operating in its survey mode, the HEA cycles through 12 V_{SA} steps every 192 ms (Yau & Howarth, 2016). Thus, in each 16-ms, fixed-V_{SA} measurement, it samples ions at 8 different incident directions, including "ram" ions from the spacecraft ram direction in the horizontal plane ($\phi_r = 0°$), "upward" ions from below the spacecraft ($\phi_u = 45°$), and "downward" ions from above ($\phi_d = –45°$). In each direction, it measures ion time-of-arrival (TOA) distributions at 8 energies-per-charge (E/q) separately, producing 64 TOA distributions in each measurement; $E/q_{min} \leq E/q \leq E/q_{max}$, $E/q_{min} \approx 0.005–0.01\ V_{SA}$, $E/q_{max} \approx 0.25–0.30\ V_{SA}$ (Yau et al., 2018).

Therefore, in each measurement at a fixed V_{SA}, each pixel samples ions over a finite E/q width (range), and the expected TOA minimum and maximum *for each ion (M/q) species* correspond to the high and low end of the E/q range, respectively. Assuming a Maxwellian energy distribution of particles, we would expect the observed time of arrival spectrum to comprise of one or more "TOA peaks", each within the expected TOA range for a certain M/q species. As demonstrated in Figure 3.3, such TOA peak regions allow for unique identification of certain species, particularly H^+, He^+ and O^+, in cases where the expected TOA ranges of adjacent species do not overlap. In the case of molecular ions, N_2^+, NO^+, and O_2^+, their TOA ranges overlap one another, but are nevertheless discernable from other species. As such, we are currently not able to resolve the exact mass composition ratio of the observed molecular ions (without further detailed and quantitative analyses), though we are able to definitively determine their presence or absence.

3.1.3 Data Products

There are several convenient ways to visualize (visually present) the measured IRM data. The first is the IRM Summary Plot (Figure 3.2 for an example), which shows the averaged ion count rate in each detector pixel as a function of time and detector pixel in each of the pixel sectors in energy-time spectrogram format (8 spectrogram panels in Figure 3.2(*a*)), and the averaged count rate over all detector pixels as a function of time and ion time of arrival in TOA-time spectrogram format (Figure 3.2(*b*)), as well as a number of derived plasma parameters as a function of time (Figure 3.2(*c*-*d*)). The Summary Plot is a useful tool for a first look at the data, especially for identifying regions or time periods of enhanced or depleted ion densities, ion upflows and downflows, and the presence of dominant or certain (for example molecular) ion species, as demonstrated in Figure 3.3 below.

To reveal the more detailed characteristics in the observed data, an algorithm was developed and implemented in IDL to present the same data in two different ways, to facilitate energy and time-based analyses of the data. The first tool, the V_{SA} Plot, provides TOA spectra (distributions) of ion count rates at individual detector pixels, helping to easily identify ion upflows and downflows as well as dominant ion species. Each TOA spectrum is plotted for four selected V_{SA} values, allowing for the simultaneous evaluation of light ions (lower V_{SA}) and more energetic or massive ions (higher V_{SA}).

When molecular ions are observed, their signatures in the V_{SA} Plot do not always look the same. Figures 3.3 and 3.4 demonstrate two of the possible cases, with distinct and coalesced peaks, respectively. While the presence of only coalesced peaks might complicate the separation of the molecular ions from the O^+, there are cases in which an O^+ peak is clearly resolved from a small second peak, which appears distinctly to the right of the O^+ peak (and its expected TOA range).

A sample of this plot is provided in Figure 3.3 in which a distinct molecular ion peak is present in Figure 3.3(*j*-*l*), with its rising edge falling to the right of the expected N_2^+ TOA range. This peak is highlighted by filling the portion of the spectrum within the TOA range with the pixel color. In comparison, Figure 3.4(*j*-*l*) show molecular ion peaks which overlap the O^+ peak, though the secondary peak and the apparent distortion of the main peak are obvious.

As a complement to the V_{SA} analysis, a Time-series Plot for time sequence analysis was also developed in IDL, an example of which is shown in Figure 3.5. This program uses a similar format to the V_{SA} analysis above, but instead of different V_{SA} values, it breaks an orbit pass or a specified time period into four equal time intervals and displays the TOA spectra of each interval. In cases of enhanced density of molecular ions over a short duration, this plot can help determine the time of the event, and therefore its geospatial location.

Finally, for comparison, Figure 3.6 shows a quiet-time example of V_{SA} Plot, in which the data were obtained during the August 2017 total eclipse. This figure is reproduced from Figure 3 in Yau et al. (2018), and it shows the TOA spectra in an alternate data display format to Figure 3.3, with the spectra for the different detector sectors superimposed and distinguished by line thickness. This orbit pass crossed the path of totality at an altitude of 640 km and at mid-latitude (at 44.3°N, 116.1°W, over Idaho), 9 minutes after totality passing.

The observed O^+ peak (right-most peak) is strongly dominated by ram ions (thick traces). This contrasts with the H^+ ions (left-most peak), which are dominated by upward ions (thin traces) in the 45° and downward ions (semi-thick traces) in the –45° sectors, respectively, with relatively negligible ram ions. This suggests the existence of two distinct H^+ ion populations or velocity components, one upward moving, having originated in the eclipsed hemisphere below, and one downward moving, originating from the non-eclipsed hemisphere or returning from a higher altitude in the eclipsed hemisphere due to loss of ion energy to gravity.

A close examination of the O^+ peak shows that the full width at half maximum (FWHM) matches precisely with the simulated instrument response. Furthermore, the complete absence of molecular ions in this quiet-time, mid-latitude orbit pass is in direct contrast to the TOA spectra in molecular ion events at high (auroral) latitudes.

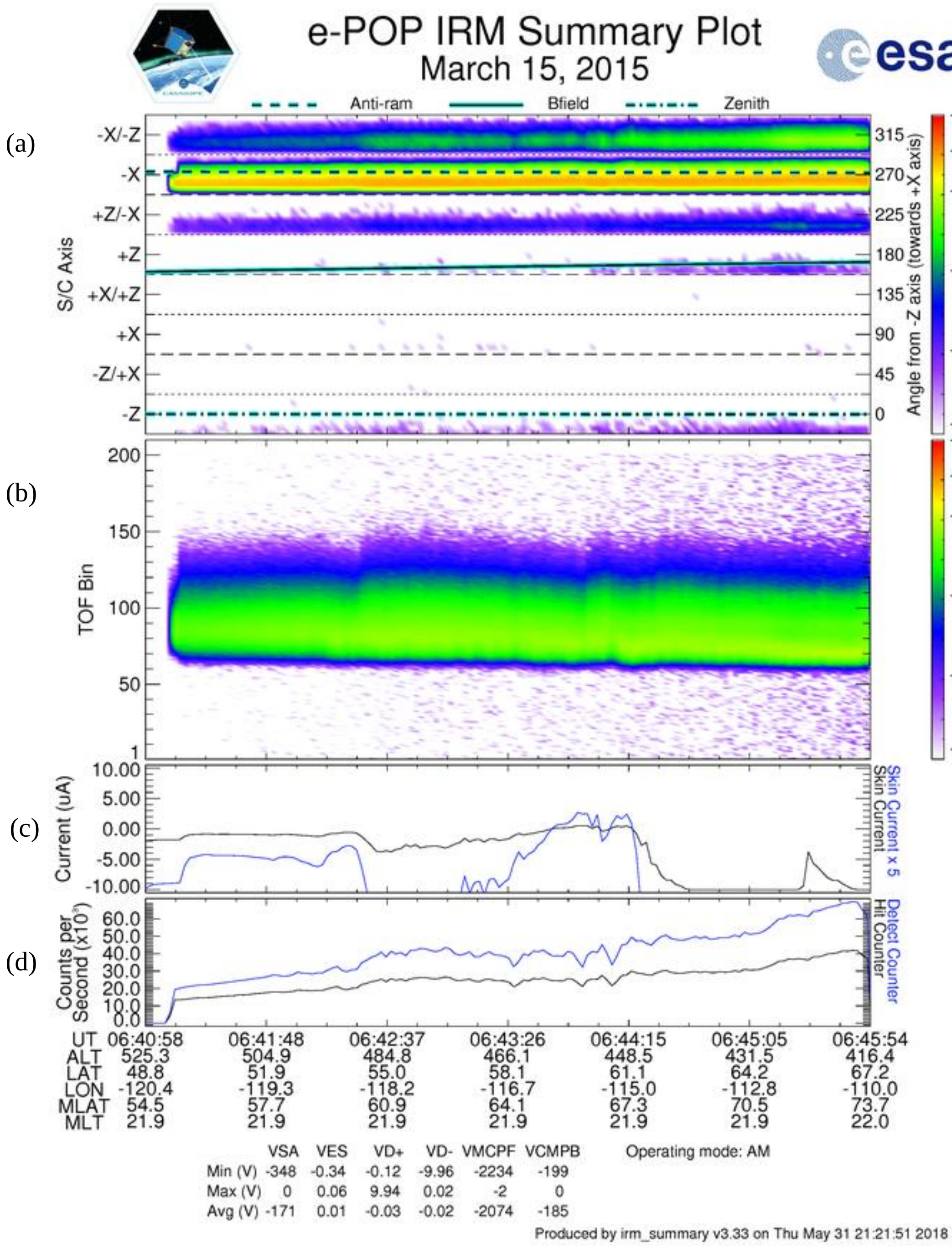

Figure 3.2: IRM summary plot. A sample of Summary Plots available on the public e-POP database for all IRM passes. Panel (a) shows the 8 energy versus time (E-t) spectrograms of averaged count rate over all TOA bins for each of the 8 detector pixel sectors and gives a quick look at the overall ion energy and azimuth distributions. Panel (b) shows the time of arrival (TOA) versus time (TOA-t) spectrogram of averaged count rate over all detector pixels, and gives a first look at the dominant ion species present. Panels (c) and (d) display the measured current on the sensor surface and the overall count rates. Together, these two parameters can be used to infer the spacecraft potential under certain geophysical conditions.

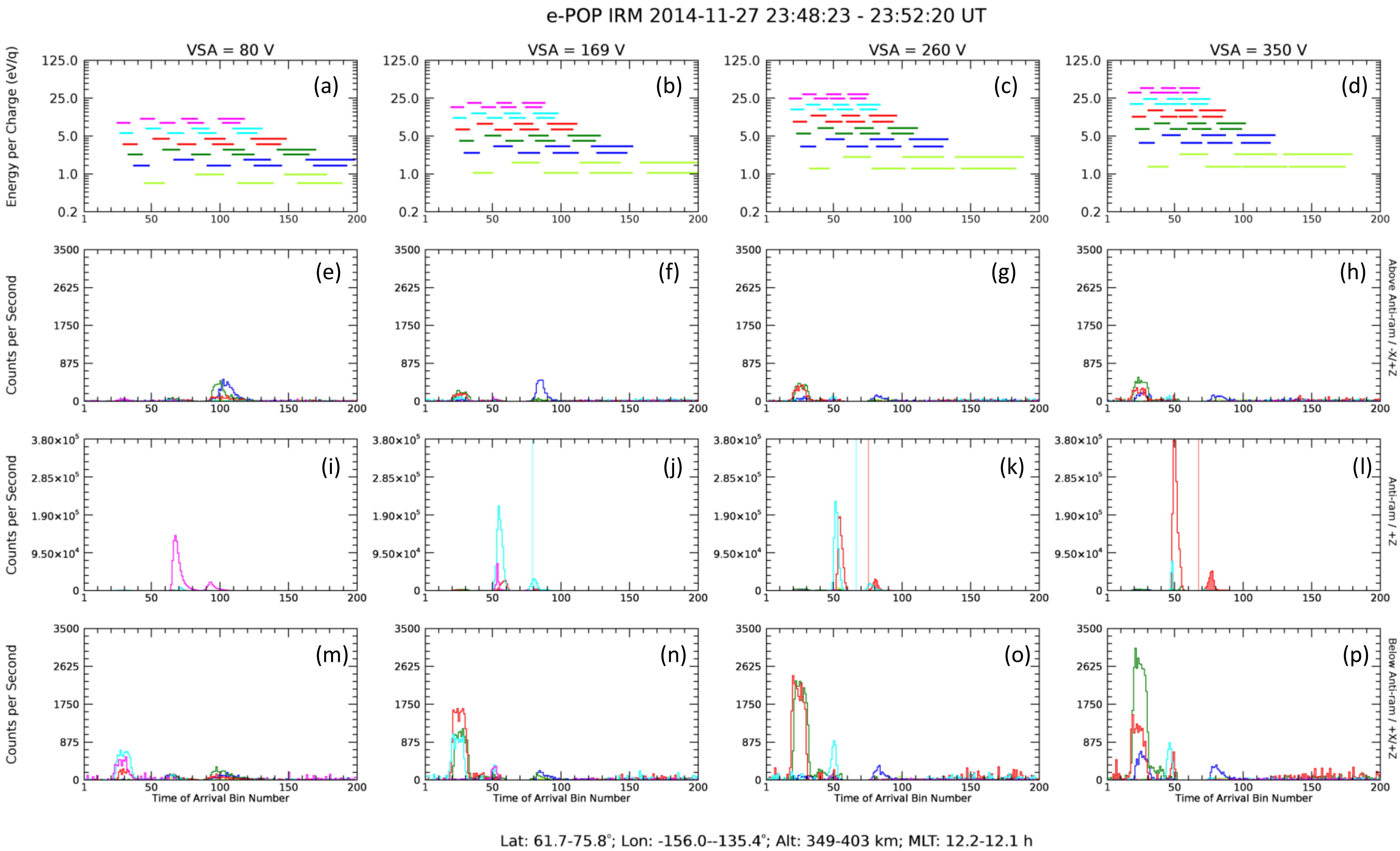

Figure 3.3: V_{SA} analysis – Distinct molecular ion peaks. A sample of data retrieved from an IRM pass. Left to right: different V_{SA} voltage bias settings; (a-d) the theoretical TOA ranges based on each pixel energy range, (e-h) the 45° upward pixel sector, (i-l) the ram pixel sector, and (m-p) the 45° down pixel sector, respectively. By extending the boundaries of each predicted TOA region downwards, it is possible to infer which species are present. In this case, panels j-l show distinct and unique peaks to the right of the N_2^+ predicted region, a clear indicator of the presence of molecular ions.

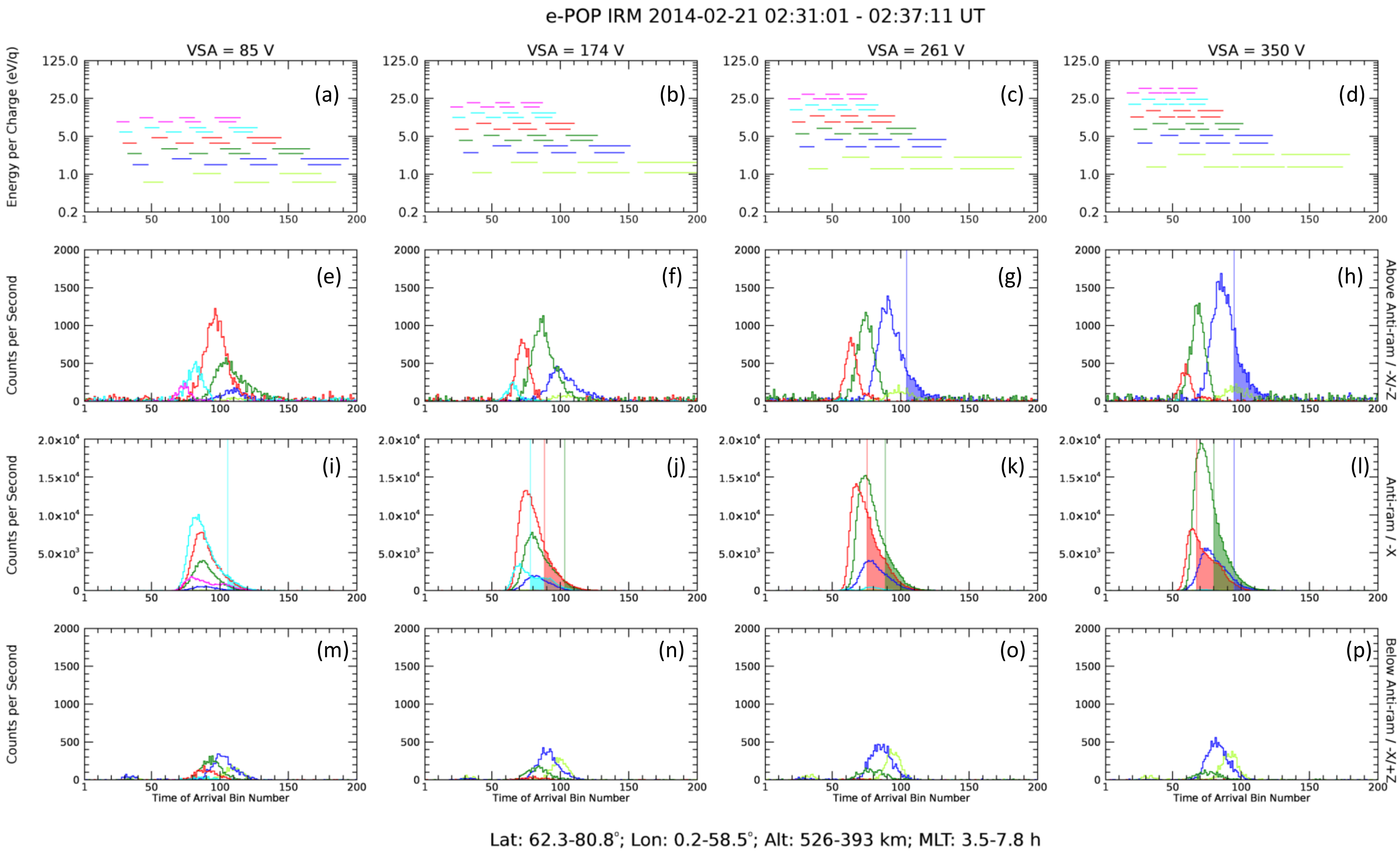

Figure 3.4: V_{SA} Analysis – Coalesced molecular ion peaks. A contrasting sample of data retrieved from an IRM pass. In this case, panels j-l show a coalesced peak to the right of the N_2^+ predicted region. The molecular ion TOA region is overlapping the O^+ peak, suggesting that the velocity distributions of the O^+ and molecular ions overlap.

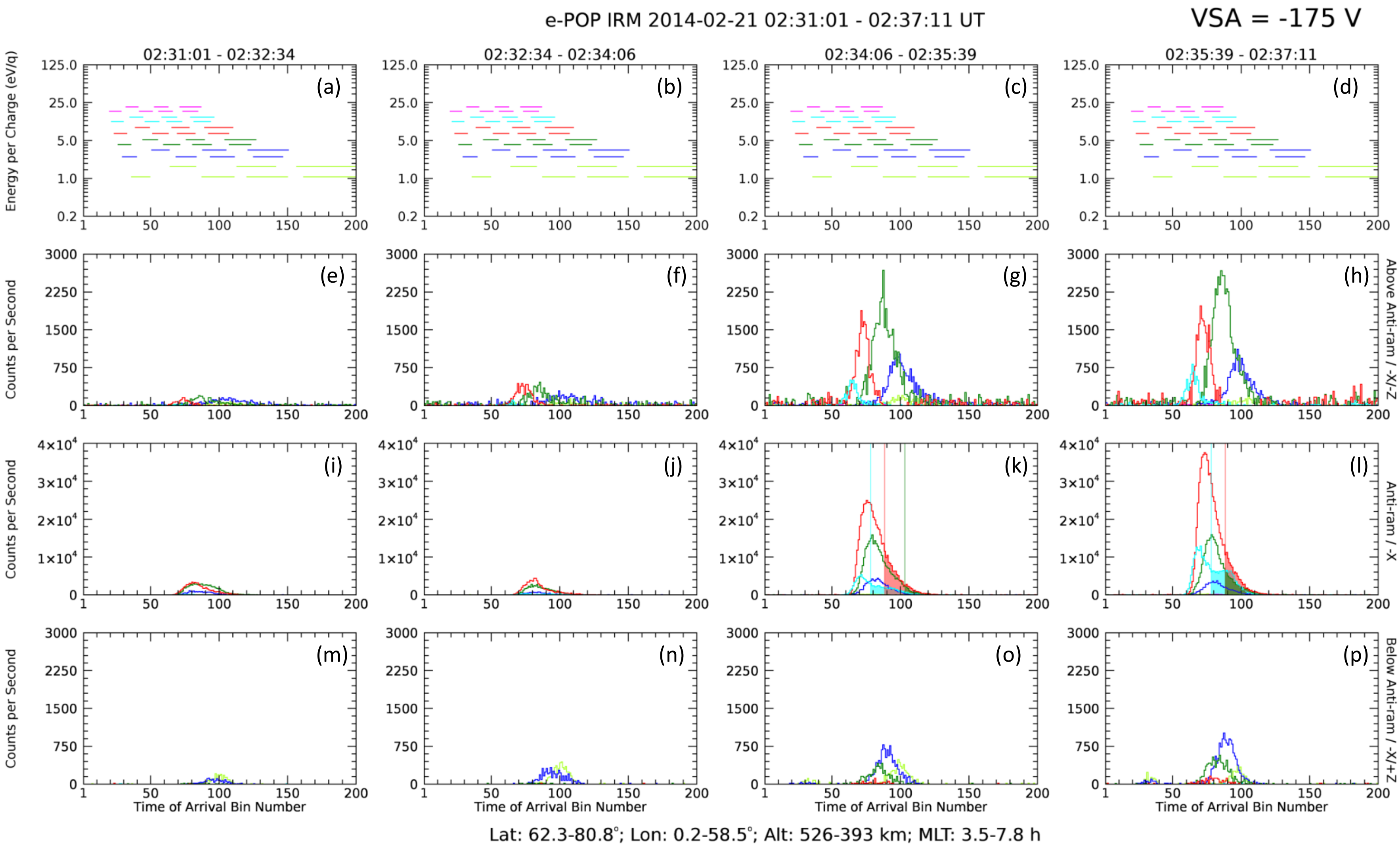

Figure 3.5: IRM time series analysis. A sample of data retrieved from an IRM pass. Left to right: different time intervals; (a-d) the theoretical TOA ranges based on each pixel energy range, (e-h) the 45° upward pixel sector, (i-l) the ram pixel sector, and (m-p) the 45° down pixel sector, respectively. This plot shows the same data plotted in Figure 3.4. It demonstrates that the molecular ions were confined to the second half of the orbit pass; this can be a useful tool when trying to spatially locate molecular ion events.

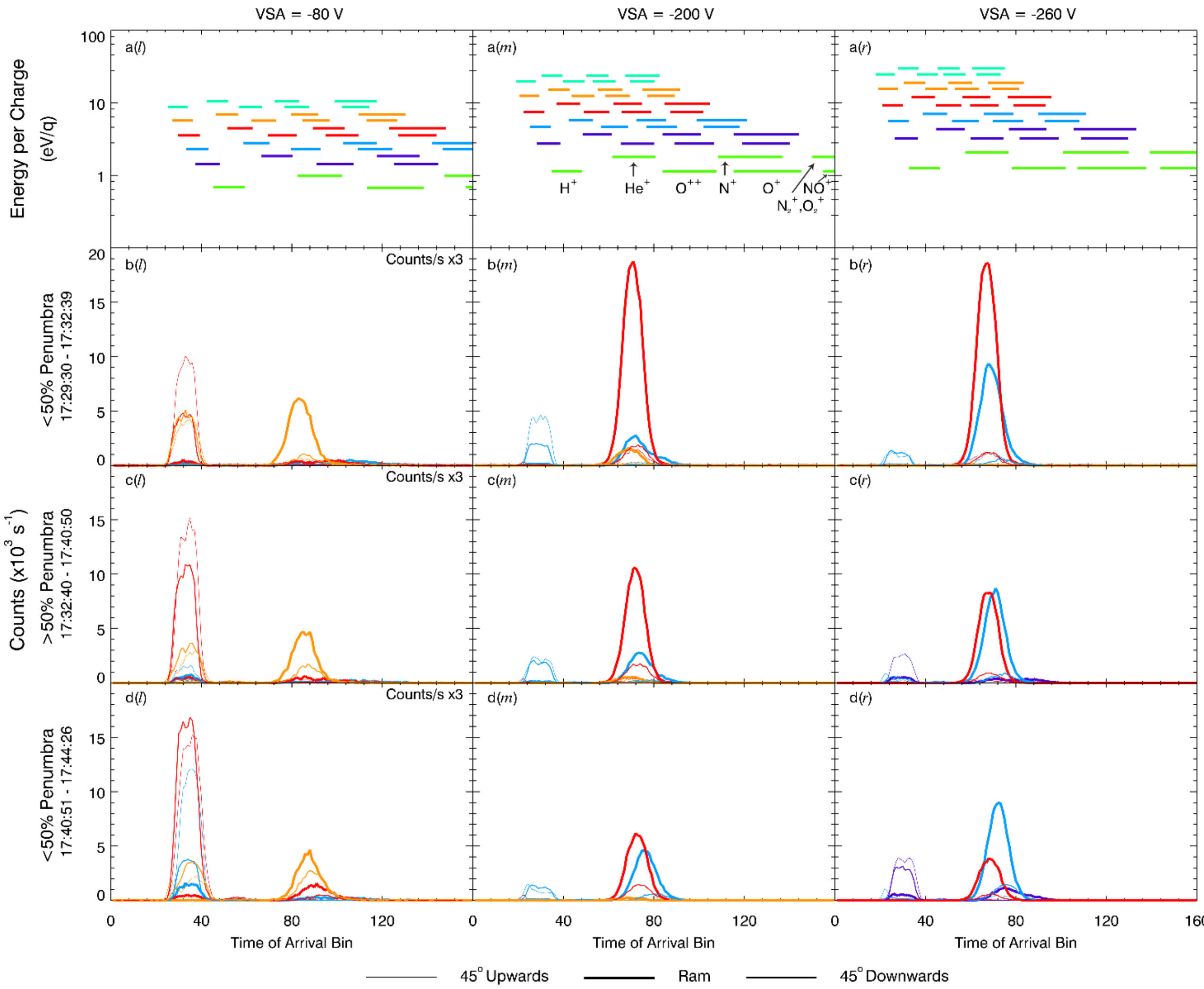

Figure 3.6: IRM August 21, 2017 Eclipse analysis. This figure is reproduced from Yau et. al (2018), and shows data obtained during the Great American solar eclipse on August 21, 2017 in an alternative data display format to Figure 3.3 and 3.4, to highlight the ionospheric changes before, during, and after the eclipse, corresponding to rows b, c, and d, respectively. In this figure we see an increase in the upward and downward flux of H^+ ions, as well as an overall density depletion marked by the steep decrease in the rightmost O^+ curve. Also of interest to this study is the complete lack of molecular ions in this magnetic quiet-time ionosphere at mid and low latitudes.

3.1.4 Data Coverage

In order to optimize the opportunity to observe plasma processes at different altitudes and local times in the topside high-latitude ionosphere with e-POP (Yau & James, 2015), the CASSIOPE was placed in an elliptical, polar orbit with an orbital inclination of 81°, a perigee of 325 km, and an initial apogee of 1500 km. The data collection for this study is limited by that which is available in the e-POP IRM database. The distribution of IRM data sampling since launch is shown in Figure 3.7, where it can be seen that the coverage is concentrated in the polar regions, and emphasizes the North American longitudinal sector (in order to maximize the opportunity for conjunctions with ground observation facilities in Canada). The coverage for the mid-latitude and equatorial regions is much more limited. This sampling distribution must be considered in the interpretation of the analysis results to be presented later as it is spatially limited.

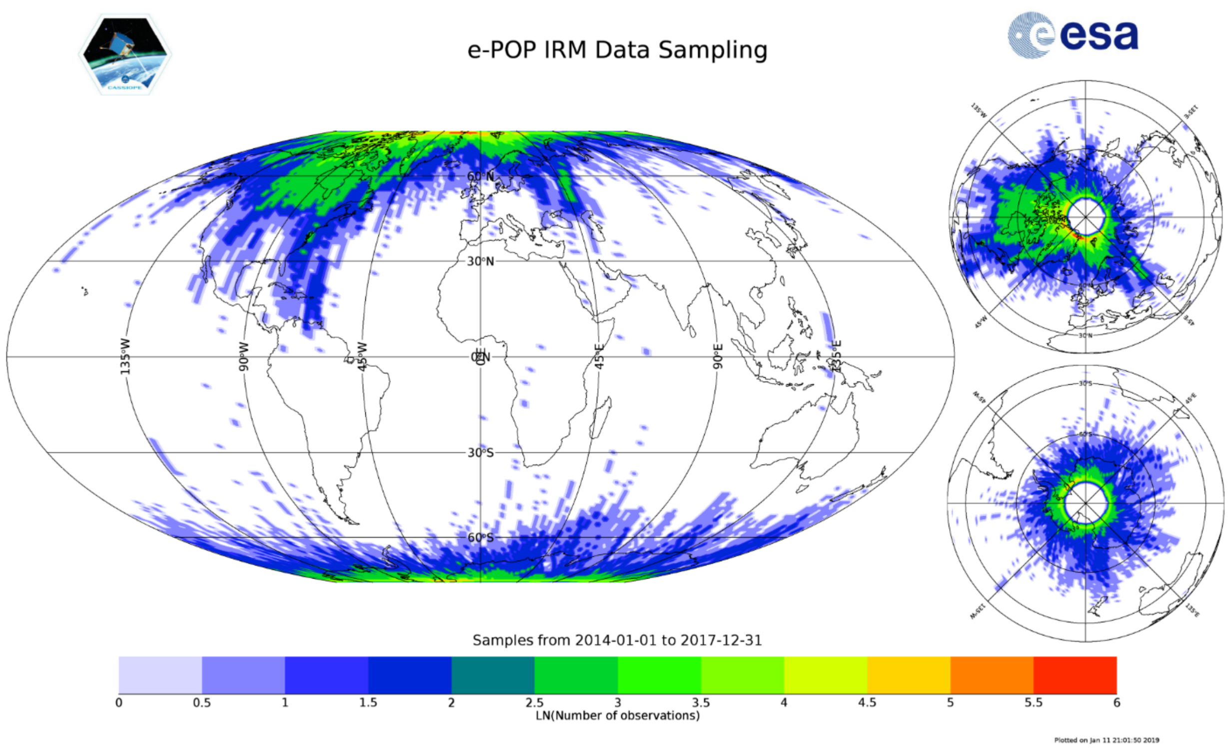

Figure 3.7: e-POP IRM data sampling. e-POP was designed to study polar and auroral processes, and as such its operation is concentrated in the Northern polar region. This occurrence frequency map shows the number of data samples taken at each geographic location since the beginning of operation.

3.1.5 IRM Analysis Methods

The IRM Instrument amassed a great deal of data over the period in question for this study, having conducted over 3000 passes in this time. Each pass can vary from less than a minute to tens of minutes in length, therefore specifying values like the geospatial spacecraft location is not possible on a pass-by-pass basis. Instead, we broke each pass down into 20 second intervals, and calculated the relevant quantities for each individual interval. An IDL program was written to extract the time, and count rates as detailed in Table 3.2 for each time interval. This provided a total of 64,810 time intervals for our analysis, or 360 hours' worth of data.

Table 3.2: Analysis data products. The following parameters were recorded for each 20 second interval of e-POP IRM data spanning from Jan 2014 to Dec 2017.

Index Number	**Data Product**
1	Year
2	Decimal Day
3	Hour
4	Minute
5	Second
6	Spacecraft Ram Angle
7	Magnetic Local Time (MLT)
8	Latitude
9	Altitude
10	O^+ Count Rate (in each of the pixel sectors 1-8)
11	Molecular Ion Count Rate (in each of the pixel sectors 1-8)
12	Molecular Ion to O^+ Ratio, 90° upwards of ram

13	Molecular Ion to O^+ Ratio, 45° upwards of ram
14	Molecular Ion to O^+ Ratio, ram
15	Molecular Ion to O^+ Ratio, 45° downwards of ram
16	Molecular Ion to O^+ Ratio, 90° downwards of ram

3.2 Hot Oxygen Simulation

In this Section, we present the detailed method for simulating the production of hot oxygen atoms via the dissociative recombination of molecular ions.

3.2.1 Boltzmann Equation

Many different types of fluid flows can be found in Earth's atmosphere. When a gas is subjected to temperature gradients, forces, and (in the case of an ionized gas) magnetic or electric fields, it will be set in motion or undergo changes to its existing motion or flow. Many mathematical theories exist which attempt to model atmospheric or ionospheric dynamics, including the Boltzmann equation. The Boltzmann equation uses a statistical approach to describe the spatial and detailed velocity distributions of a particle population, and it can be used to analyze the macroscopic properties of a gas such as pressure and temperature.

In the case of our simulation, we consider the dissociative recombination of O_2^+ and NO^+ using the linearized Boltzmann equation, and calculate the velocity phase space density distribution of the resulting hot oxygen atoms in each case separately. A rigorous kinetic simulation using the full, 3-dimensional Boltzmann equation and involving multiple production processes in the transition altitude region between the collisional E-region and the non-collisional topside ionosphere is very difficult to solve even numerically. It was shown by Kabin and Shizgal (2002) that a one-dimensional local Boltzmann equation yields a similar result in the case of the exosphere of Venus. The model correctly predicted the well-known two temperature exosphere and temperature profiles in agreement with Monte Carlo simulations by Hodges (2000).

We want to use the Boltzmann equation to find the velocity distribution that would result from the initial production and subsequent collisional relaxation of the hot oxygen atoms. Such a formulation must include the effects of gravity, collisions, and atomic oxygen production. A detailed derivation was presented in Kabin and Shizgal (2002) under the assumption that the source of atomic oxygen is spherically symmetric, and the equation is given by:

$$\frac{\partial f}{\partial t} + v \cdot \nabla_r f_v + \frac{G(r)}{m} \cdot \nabla_v f = J[f] + Q(v) \qquad [3.1]$$

For our purposes, we assume the first term, $\partial f / \partial t$ is zero. While the velocity distribution likely does change with time, we consider in our study the "steady-state" distribution at some time *t* after collisional relaxation, so we can discard this term. The second term, $v \cdot \nabla_r f_v$, describes how the velocity distribution changes with altitude and we will integrate this term to find our final solution at a given altitude. The third term, $\frac{G(r)}{m} \cdot \nabla_v f$ is the deceleration of the particles due to gravity, where:

$$G(r) = -\frac{GmM_E\vec{r}}{r^3} \qquad [3.2]$$

where G is the universal gravitational constant (G = 6.67×10^{-11} $m^3kg^{-1}s^{-2}$), m the mass of the oxygen atom, M_E is the mass of the Earth (M_E = 5.972×10^{24} kg), and r the geocentric distance. Finally, on the right hand side of the equation we have *J*[*f*], the collision operator and the source distribution term, *Q(v)*, which will be discussed in greater detail in the next section (3.2.2). The collision operator is given by:

$$J[f] = \int_0^\infty K(v', v) f(v') dv' - Z(v) f(v) \qquad [3.3]$$

where $K(v', v)$ is the collision kernel, which reduces to a simple form (Hoare & Kaplinsky, 1970) in the case of a hard sphere collision:

$$K(x, y) = A\sqrt{\frac{\pi}{x}}\,\mathrm{erf}\left(\sqrt{y}\right) \quad y < x; \qquad [3.4a]$$

$$K(x, y) = A\sqrt{\frac{\pi}{x}}\exp(x - y)\,\mathrm{erf}\left(\sqrt{x}\right) \quad y > x \qquad [3.4b]$$

where

$$x = \frac{mv^2}{2k_B T} \qquad [3.5a]$$

$$y = \frac{mv'^2}{2k_B T} \qquad [3.5b]$$

$$A = n_0 \sigma_{HS}\sqrt{\frac{k_B T}{2m}} \qquad [3.5c]$$

n_0 is the density of ambient gas, and all other terms are as previously defined. σ_{HS} is the hard-sphere collision cross section and $Z(v)$ is the collision frequency:

$$Z(v) = A\left\{\left(2\sqrt{x} + x^{-\frac{1}{2}}\right)\frac{\sqrt{\pi}}{2} + \exp(-x)\right\} \qquad [3.6]$$

For the preliminary simulations, the density profiles were obtained from the IRI-2007 and MSISE-00 models. Later, augmented models were developed based on e-POP observations, and are discussed in subsequent sections. Once all parameters of the simulation are established, each of the terms can be calculated, as depicted in Figure 3.8.

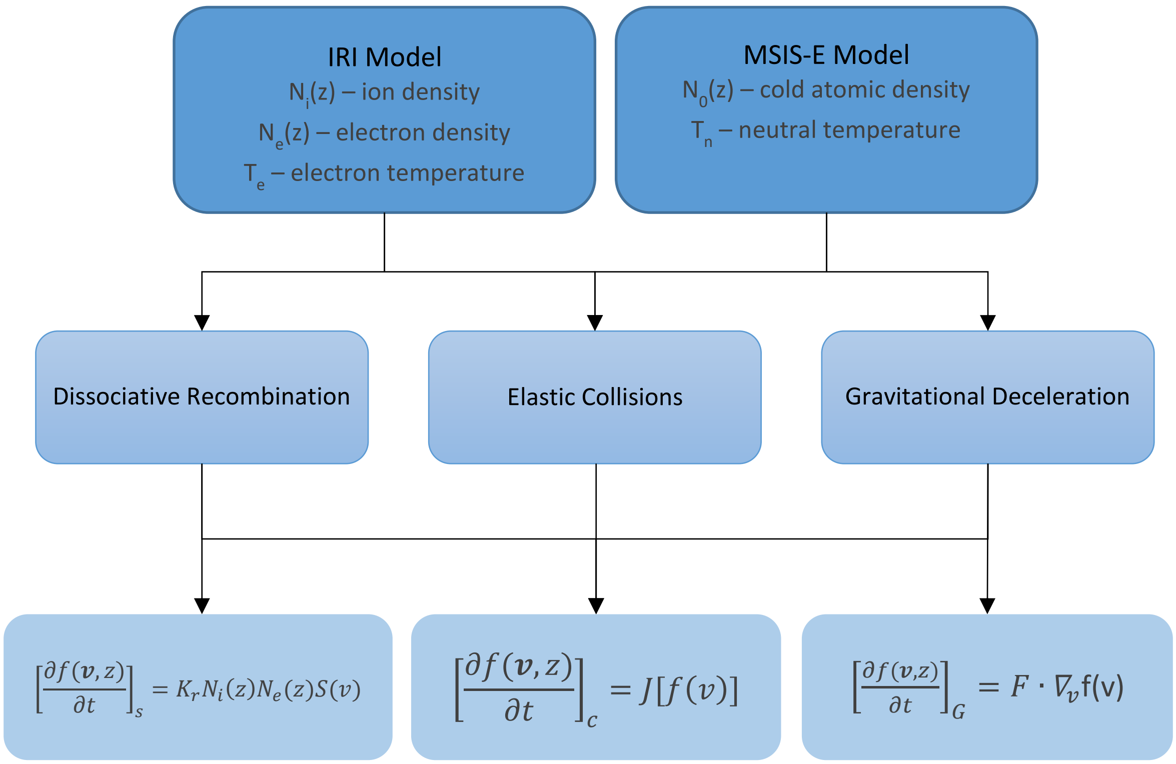

Figure 3.8: Boltzmann Equation Terms. Setting up the solution to the Boltzmann equation requires inputs from both neutral and ion models as shown here. A further term, the source velocity distribution term S(v), is required for the complete solution and is discussed in Section 3.2.2.

3.2.2 Molecular Ion Source Function

To determine the initial velocity distribution of the hot oxygen atoms produced by the dissociative recombination (part of the source velocity distribution term $Q(v)$ in equation [3.1]), we can use the theory of bimolecular reactions following the formulation of Whipple (1974), which is generalized in the form:

$$m_1 + m_2 \rightarrow m_3 + m_4$$

where m_1 and m_2 denote the reactant species and m_3 and m_4 the product species. We assume that the velocity distributions of species 1 and 2 are Maxwellian in nature, at some temperature T:

$$f_i = N_i \left(\frac{m_i}{2\pi k_B T}\right)^{\frac{3}{2}} exp\left(\frac{-m_i v_i^2}{2k_B T}\right) \qquad [3.7]$$

where N_i is the concentration and m_i is the mass of incident species i, k_B the Boltzmann constant, and T the ambient temperature.

The problem applies to any arbitrary hard sphere cross section, σ_{HS}, of the reactants, so long as one can assume that the scattering of the product particles is isotropic. The reaction energy, E_R, values of which are given in Table 2.1, is the difference between the kinetic energies of the products and reactants, and is positive in the case of an exothermic reaction, negative in the case of an endothermic reaction. If f_3 is the resulting velocity phase space distribution of interest, then the rate of change of that distribution is given by:

$$\frac{\partial f_3}{\partial t} = \frac{4\sigma_{HS} N_1 N_2 m_3^2}{\pi v_3 \sqrt{2k_B T m_1 m_2 m_4}} \exp\left[\frac{-m_3 v_3^2}{2k_B T} + \frac{E_R}{k_B T}\right] F(x_3, x_0) \qquad [3.8]$$

where

$$\begin{aligned} F(x_3, x_0) = \frac{\sqrt{\pi}}{2}\left[\frac{1}{2} + x_3^2 - x_0^2\right]\left[erf\left(x_3 + x_0\right) + erf\left(x_3 - x_0\right)\right] \\ + \frac{1}{2}\left(x_3 + x_0\right)\exp\left[-\left(x_3 - x_0\right)^2\right] + \frac{1}{2}\left(x_3 - x_0\right)\exp\left[-\left(x_3 + x_0\right)^2\right] \end{aligned} \qquad [3.9]$$

and

$$x_3 = v_3 \left(\frac{m_4}{2k_B T}\right) \quad [3.10a]$$

and

$$x_0^2 = \frac{m_3+m_4}{m_3}\frac{E_R}{k_B T} \quad [3.10b]$$

In the case where there are many possible branches for a reaction, the total distribution can be expressed by scaling the distribution relative to the appropriate branching ratio and superimposing solutions obtained for each reaction energy.

We then use this to formulate our source distribution, where

$$S(v) = 4\pi v_3^2 \left(\frac{\partial f_3}{\partial t}\right) \quad [3.11]$$

The velocity distributions can be converted easily into energy distributions under the assumption that the velocity and energy are related by the kinetic energy equation:

$$E = \frac{mv^2}{2} \quad [3.12]$$

We then use this to formulate the source function discussed in the previous section:

$$Q(r,v) = K_r \, N_{O_2^+}(r) \, N_{e^-}(r) \, S(v) \quad [3.13]$$

where N_{O2+} (r) or N_{NO+} (r) and N_{e-} (r) denote the altitude dependent ion and electron number densities, respectively, and K_r the recombination rate coefficient (Sheehan & St. Maurice 2004):

$$K_r(\mathrm{NO}^+) = 3.5\times10^{-7}\left(\frac{300}{T_e}\right)^{0.69} \quad [3.14a]$$

$$K_r(\mathrm{O}_2^+) = 1.95\times10^{-7}\left(\frac{300}{T_e}\right)^{0.7} \qquad [3.14b]$$

Taking into account the branching ratios of the respective dissociative recombination product channels (Table 2.1), the resulting energy distributions from the dissociative recombination of NO^+ and O_2^+ are given in Figure 3.9 and Figure 3.10, respectively.

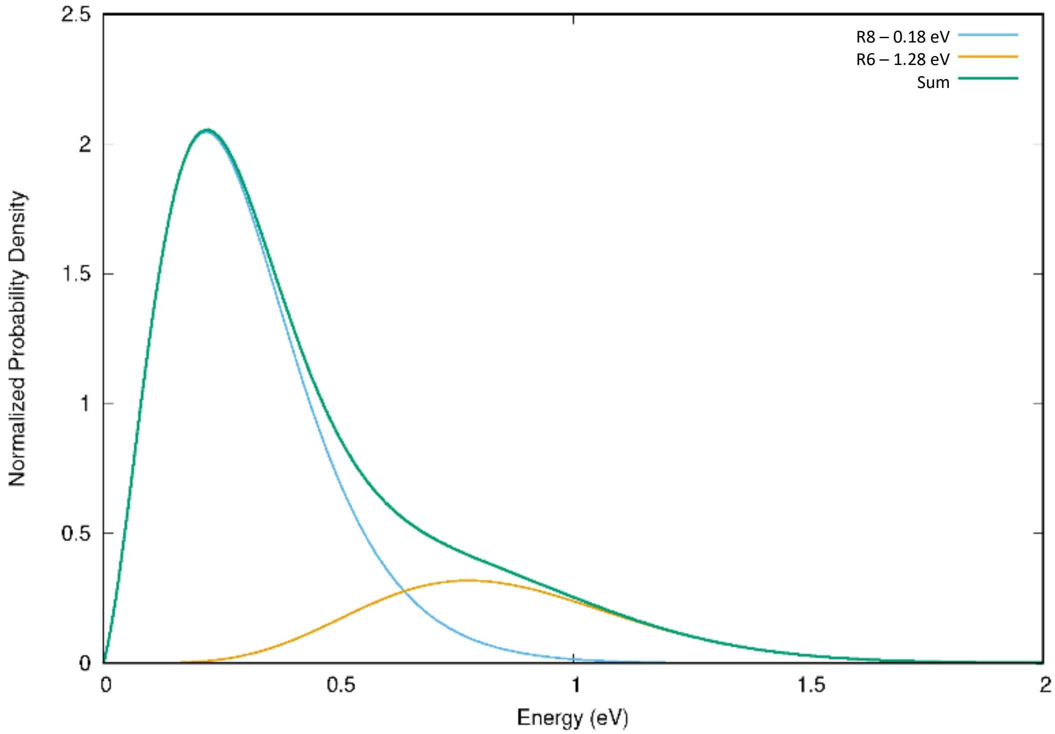

Figure 3.9: Energy distribution from NO^+ recombination. The energy distribution of atomic oxygen which results from the dissociative recombination of NO^+. The low energy peak dominates in this case, with a much smaller average energy compared to the O_2^+ recombination reaction in the next figure.

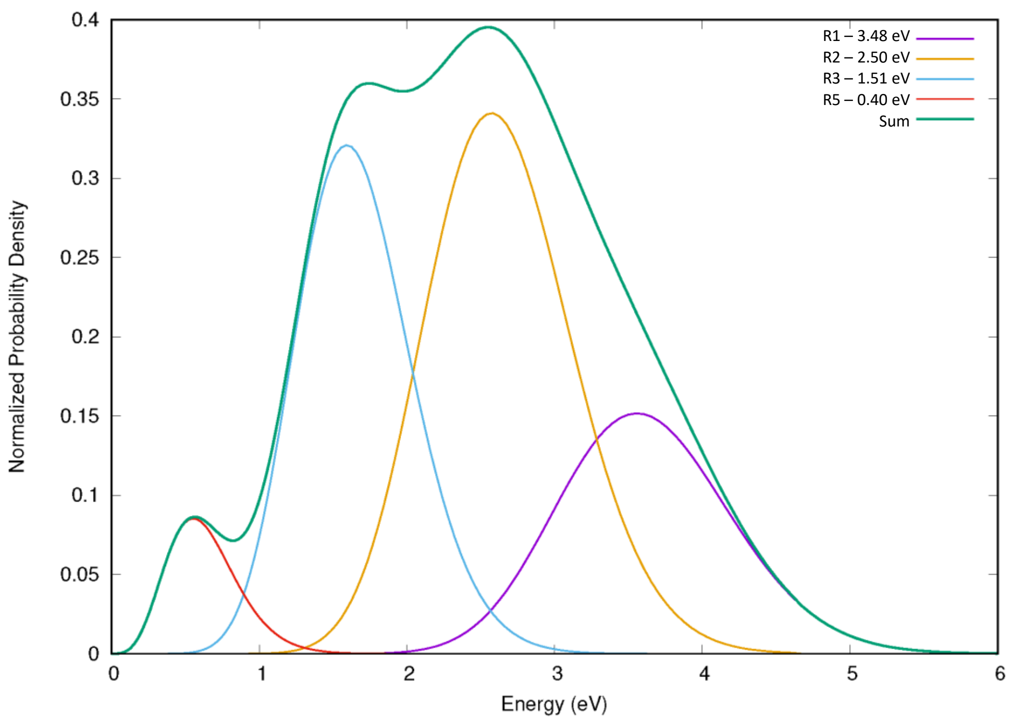

Figure 3.10: Energy distribution from O_2^+ recombination. The energy distribution of atomic oxygen which results from the dissociative recombination of O_2^+. The exothermicities of these reactions are much higher than in the NO^+ case, and this distribution has a much higher average energy.

3.2.3 Solution Algorithm

The process of solving the linearized Boltzmann equation [3.1] above was carried out previously by Kabin and Shizgal (2002) in their study of the Venus exosphere. Their Fortran 77 code was converted to Fortran 95 and modified for the purposes of this study.

In particular, the first simulation uses the MSIS and IRI as input models for densities and temperatures, and the Whipple source distribution (equation [3.8-3.11]) and the rate coefficients in equation [3.14] for calculating the source function (equation [3.13]). Other simulations use modified IRI profiles which are discussed in Chapter 4.3.

The program uses an iterative approach, solving the equation for the phase space density at a given altitude, and using that solution as the starting point for the next discrete altitude level. This process is demonstrated by the flow chart in Figure 3.11.

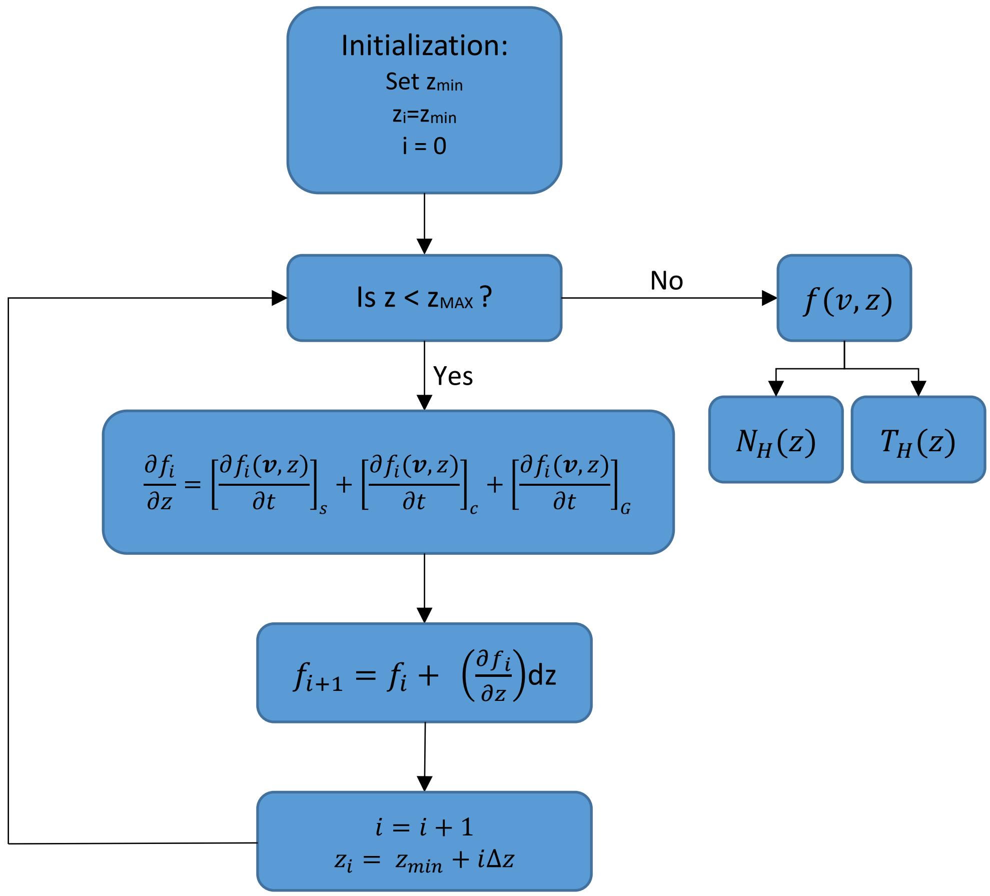

Figure 3.11: Hot oxygen simulation solution algorithm. This iterative approach was used to solve for the atomic oxygen energy distribution at each altitude, from which the density of hot atoms $N_H(z)$ and the resulting hot temperature $T_H(z)$ can be derived through integration and slope analysis, respectively. All other terms are described in Section 3.2.1.

4 Results

In this Chapter, we present the analysis results of molecular ion occurrence morphology with respect to magnetic local time (MLT) (Section 4.1) and various solar and geophysical indices (Section 4.2), using the observation data from the imaging and rapid-scanning ion mass spectrometer (IRM) instrument. We then present the simulation results of the production of hot atomic oxygen via the dissociative recombination of molecular ions (Section 4.3).

4.1 MLT Distributions of Molecular Ions

Many common coordinate systems are fixed to the Earth, though sometimes a system with respect to the position of the Sun is more convenient. Magnetic local time (MLT) is the hour angle (1 hour corresponds to 15° magnetic longitude) from the midnight magnetic meridian. The MLT coordinate system then rotates relative to the Earth, but is stationary in the Earth-Sun reference frame.

As shown in Table 3.2, the magnetic local time, magnetic latitude, and count rates of both O^+ and molecular ions are recorded for each IRM data sample. To investigate the MLT dependence of molecular ion occurrence, the observed molecular ion events were first categorized by event size and then ranked in terms of count rates. Events with more than 15,000 counts/s were considered *large* count rate events, events with count rates of 10,000 - 15,000 counts/s *medium* count rate events, and finally, events with count rates of 5,000 - 10,000 counts/s were considered *small* count rate events.

The three categories of observed events were then plotted in a magnetic latitude and MLT coordinate system, as shown in Figure 4.1. There is a concentration of large count rate events in the pre-midnight sector, though no other trends are immediately apparent. The detailed distributions of events in Figure 4.1 are summarized in Table 4.1 in terms of the number of events in each category and 2-hr MLT sector.

The e-POP data sampling is highly concentrated at high latitudes in the northern hemisphere (cf. Figure 3.7). So, when considering an occurrence frequency distribution in the data, it is important to take into consideration the distribution of data sampling. Figure 4.2 shows the occurrence of small, medium and large count rate events as a percentage of total data samples as a function of MLT. We see that indeed the large count rate events are concentrated within the pre-midnight sector, while the smaller events peak in the 8-10 MLT sector.

Table 4.1: MLT distributions of molecular ions. Presented are the detailed abundance of molecular ion events in each 2-hour MLT sector.

MLT Sector	Small Events	Medium Events	Large Events	Less than 5000 counts/s
0-2	337	114	36	8194
2-4	223	96	43	6125
4-6	174	101	44	5150
6-8	160	74	20	3879
8-10	324	46	3	3314
10-12	153	32	8	4464
12-14	255	111	67	4213
14-16	237	32	10	3552
16-18	289	56	17	4361
18-20	280	62	29	3830
20-22	181	86	310	5214
22-24	345	119	124	7916

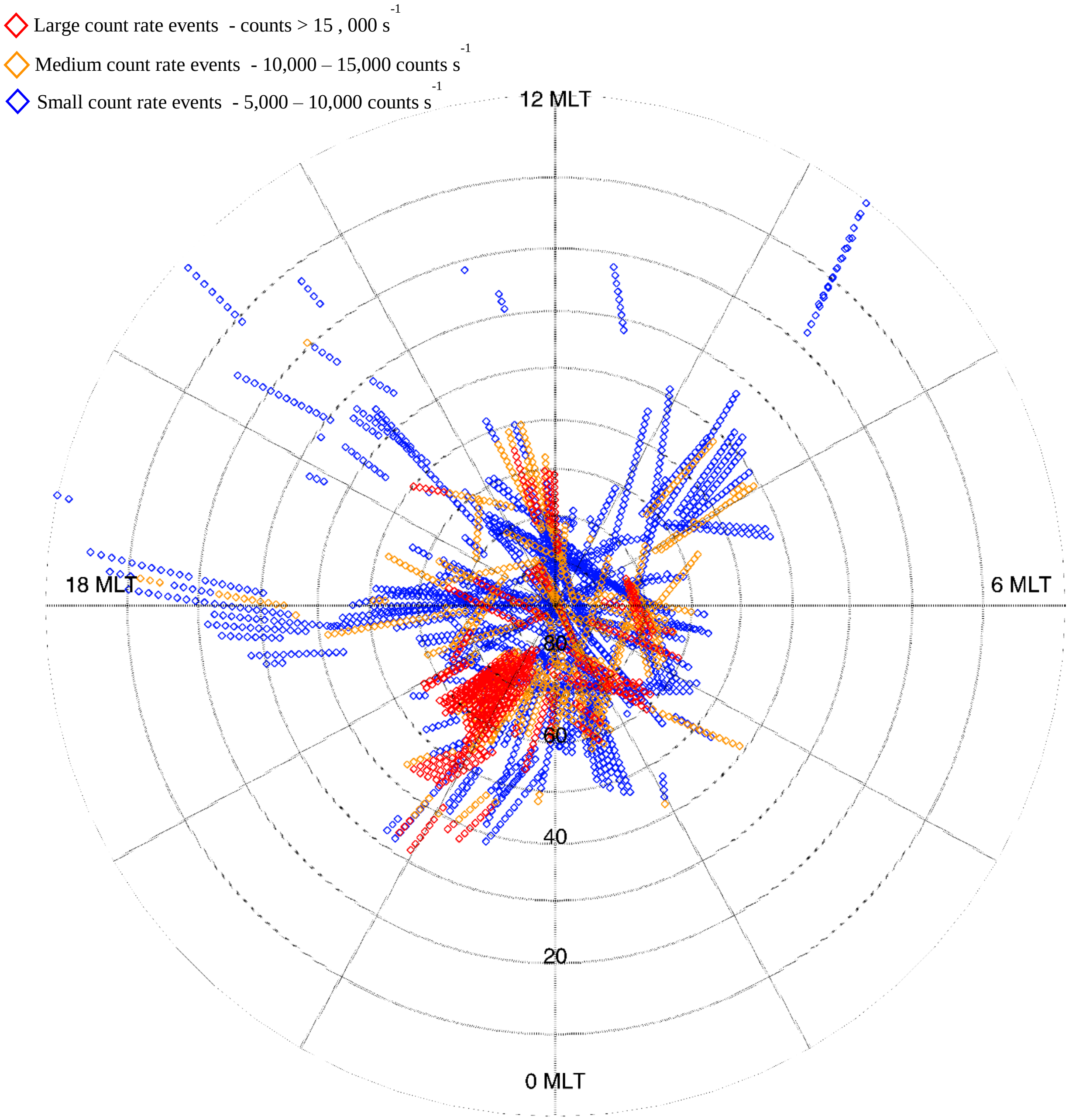

Figure 4.1: MLT distributions of molecular ions. Individual events of molecular ions are shown versus magnetic latitude and MLT. A small, medium, and large event is where the count rate is between 5,000 and 10,000, between 10,000 and 15,000, and higher than 15,000 counts/s, respectively. The 4-8 MLT sector shows a relative lack of events below 60° magnetic latitude due to under-sampling.

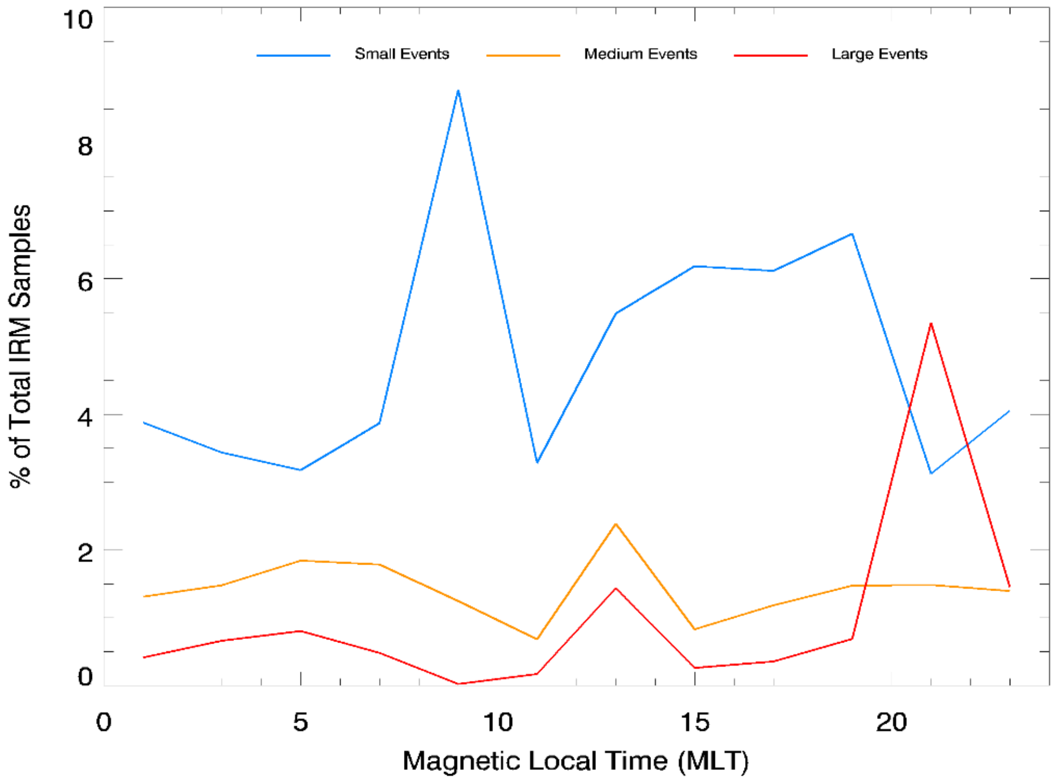

Figure 4.2: Molecular ion occurrence frequency. The occurrence frequency of molecular ions in each 2-hour MLT sector is shown for small, medium, and large count rate events. The frequency for large events peaks in the 20-24 MLT sector, while the frequency for small events peaks in the 10-12 MLT sector.

4.2 Correlation to Solar Activity Indices

4.2.1 AE

As a first look at any possible correlation between the AE index and molecular ions, we present Figure 4.3 and 4.4, which show the count rates of molecular ions and the molecular ion to O^+ count rate ratios, respectively, versus the AE index. In each figure, panel (a)-(c) show the data in the upward, ram and downward pixel sectors, respectively, in scatter plot format. In each panel, the individual data points are color coded by F10.7.

A quick glance at the results suggests that molecular ions are not only present at active times, as suggested by previous studies of energetic upflowing molecular ions at higher altitudes (e.g.

Peterson et al., 1994), but they are in fact also regularly observed at all AE index values to varying degrees. Panel (d) in each figure highlights the underlying trends in the data set. Each of the >64,000 data samples was binned into AE bins of 100 nT in width, and the average of all samples in each bin was calculated.

Figure 4.3(d) shows that the upward and downward count rates of molecular ions are approximately equal, with the upward rates being slightly larger. This may suggest that a small fraction of the upward ions is accelerated further above the F region, where they reach escape energy and do not return to the atmosphere, as discussed in Yau & Andre (1997). The average count rates (Figure 4.3(d)) are more or less constant with AE, with an increase in the upward and ram sectors around AE at 700.

Figure 4.4(d) shows that the overall molecular ion to O^+ count rate ratio decreases with AE in all three directions (detector pixel sectors). The apparent decrease in this ratio is attributed to (i.e. believed to reflect) the larger N^+/O^+ ratio that is found to accompany molecular ion events at active times. Since the N^+ and O^+ TOA ranges of the measured ions overlap (cf. Figure 3.3-3.6, top row), an increased N^+/O^+ ratio due to an increased N^+ density would increase the contribution of N^+ ions to the measured ion count rate in the O^+ TOA range, and result in a corresponding decrease in the calculated molecular to O^+ ion ratio in the case of unchanged O^+ density.

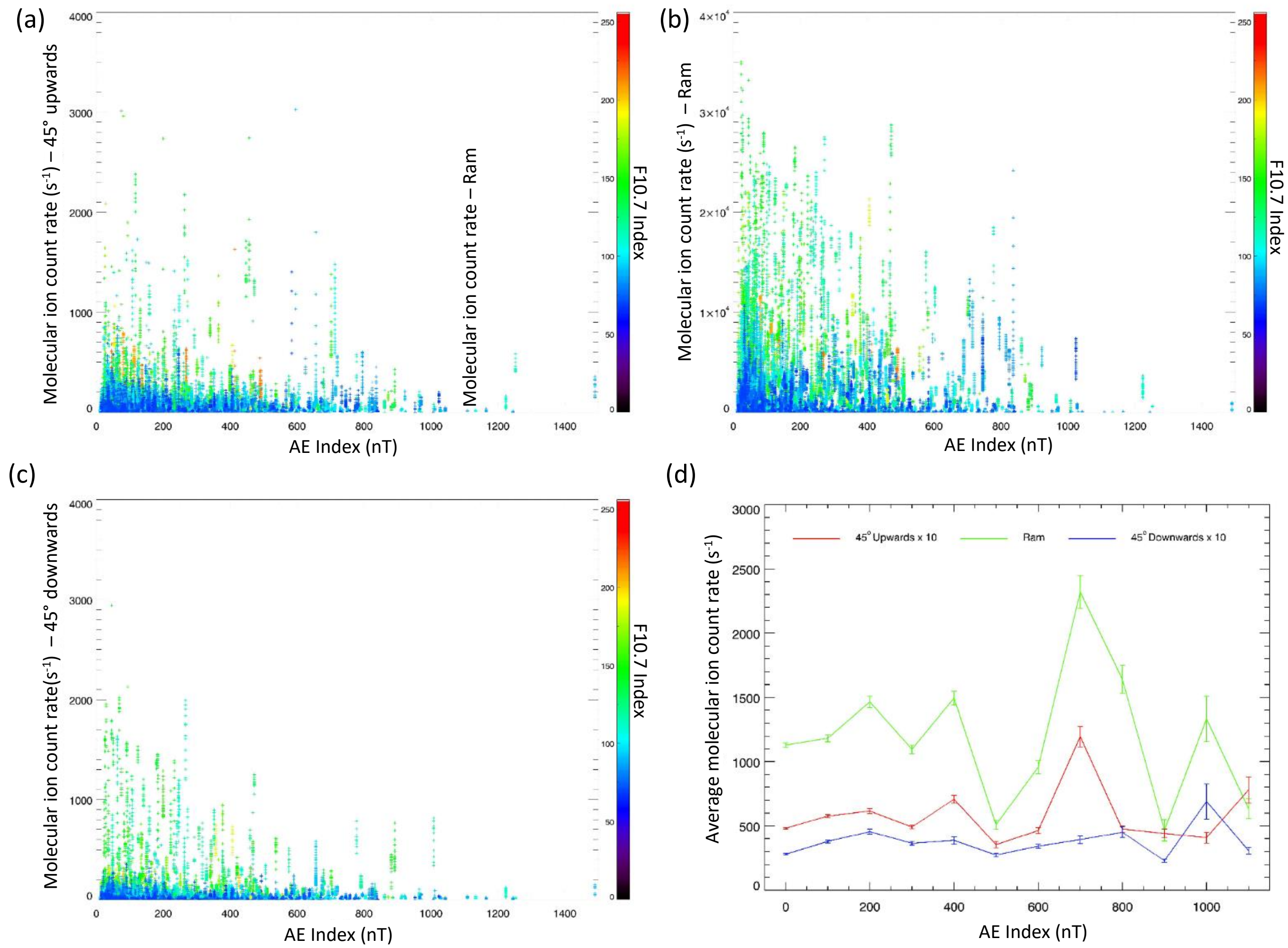

Figure 4.3: Molecular ion count rates versus the AE index. (a) the (45°) upward sector, (b) the ram sector, and (c) the (–45°) downward sector. (d) the average count rate in each 100 nT AE bin. Count rates of upward and downward molecular ions are relatively constant, though ram ions show a peak around 700 nT.

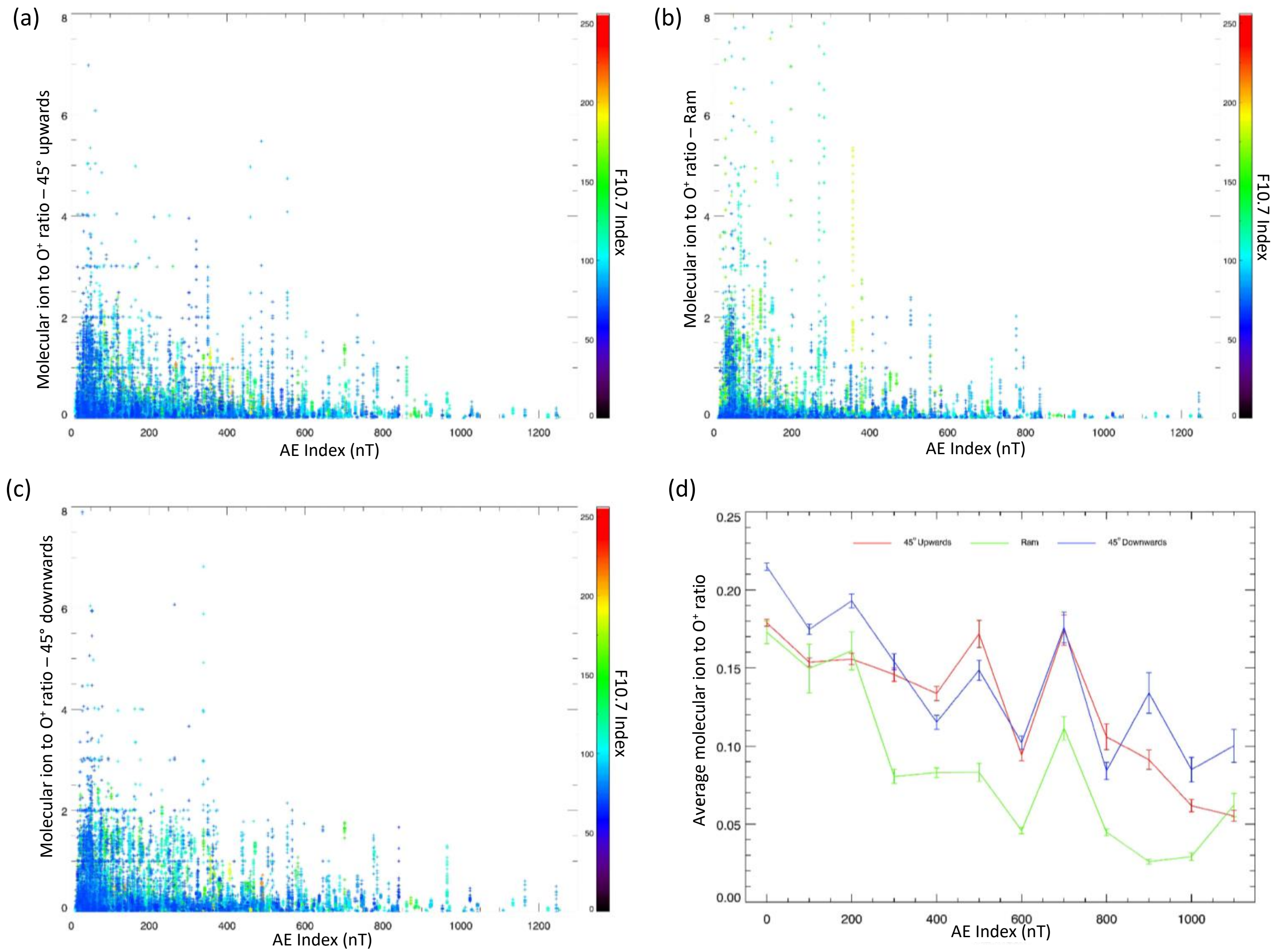

Figure 4.4: Molecular ion to O$^+$ ratio versus the AE index. (a) the (45°) upward sector, (b) the ram sector, and (c) the (–45°) downward sector. (d) the average ratio in each 100 nT AE bin. The ratios appear to decrease with increasing AE index.

4.2.2 KP

We now present a similar analysis to the previous section, but this time in terms of the Kp index. Both the count rates and molecular ion to O^+ ratios are plotted against the Kp index, and the individual data points are color coded by F10.7 in panels (a)-(c). Similar to the case of the AE index in Figure 4.3 and 4.4, the average molecular ion to O^+ ratio decreases as Kp increases. Unlike the case of AE index, however, the average count rate shows a distinct increase with Kp, particularly in the ram sector.

Again, we see a correlated flux of both upward and downward ions, with slightly more ions moving upward than downward, indicating that a small fraction of the ions are being accelerated upward to beyond escape energy and manages to escape, as discussed above.

4.2.3 DST

Finally, we assess the occurrence frequency of the molecular ion count rate and molecular ion to O^+ ratio as a function of the Dst index. As discussed in section 1.3.2.1, a geomagnetic storm has multiple (3) phases. We pose the question as to whether or not the observed molecular ions are in any way connected to the phase of a given storm. To analyze this, hourly Dst index values were retrieved from the OmniWeb Service provided by NASA. The Dst time series for the entire four-year data period (from January 2014 to December 2017) was plotted, and large, medium and small-scale molecular ion events (as defined previously) were identified using the same color coding scheme. It is important to mention that the total sample set is relatively uniformly distributed across multiple storm phases, seasons and years.

Figure 4.7 shows that large count rate events seem to occur more frequently in the presence of large solar storms, particularly during the recovery phase. The large solar storm in Spring 2015 contains 36/46 of the entire years’ large count rate events. The relatively small number of large count-rate events overall is attributed to the fact that our data period (2014-2017) happens to be near solar minimum, when relatively few large storms occurred. The year of 2016, for example, did not see a single event with molecular ion count rates above 15,000 ions/s.

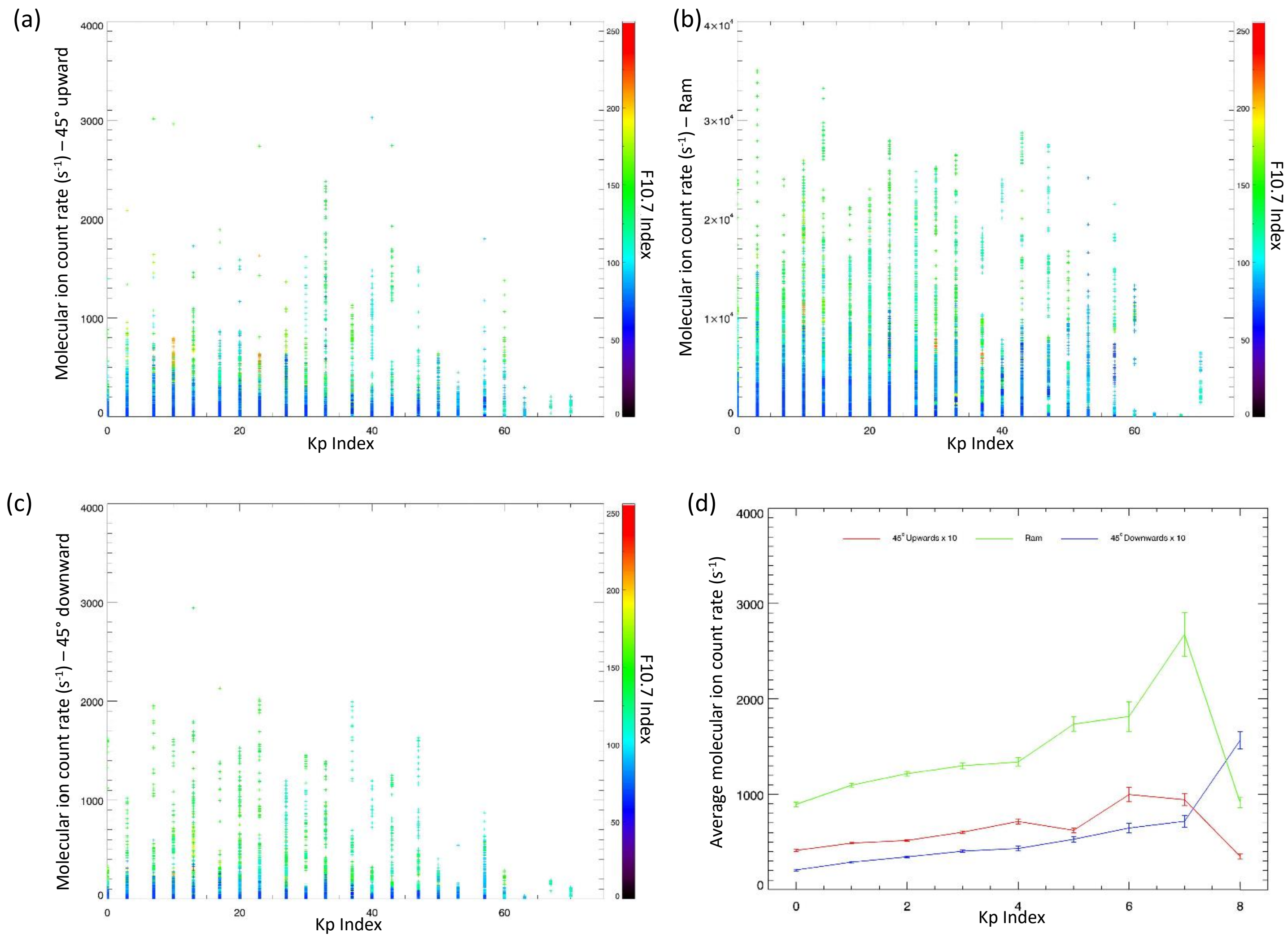

Figure 4.5: Molecular ion count rates versus the Kp index. (a) the (45°) upward sector, (b) the ram sector, and (c) the (–45°) downward sector. (d) the average count rate in each Kp bin. The molecular ion count rates seem to increase with an increase in the Kp index.

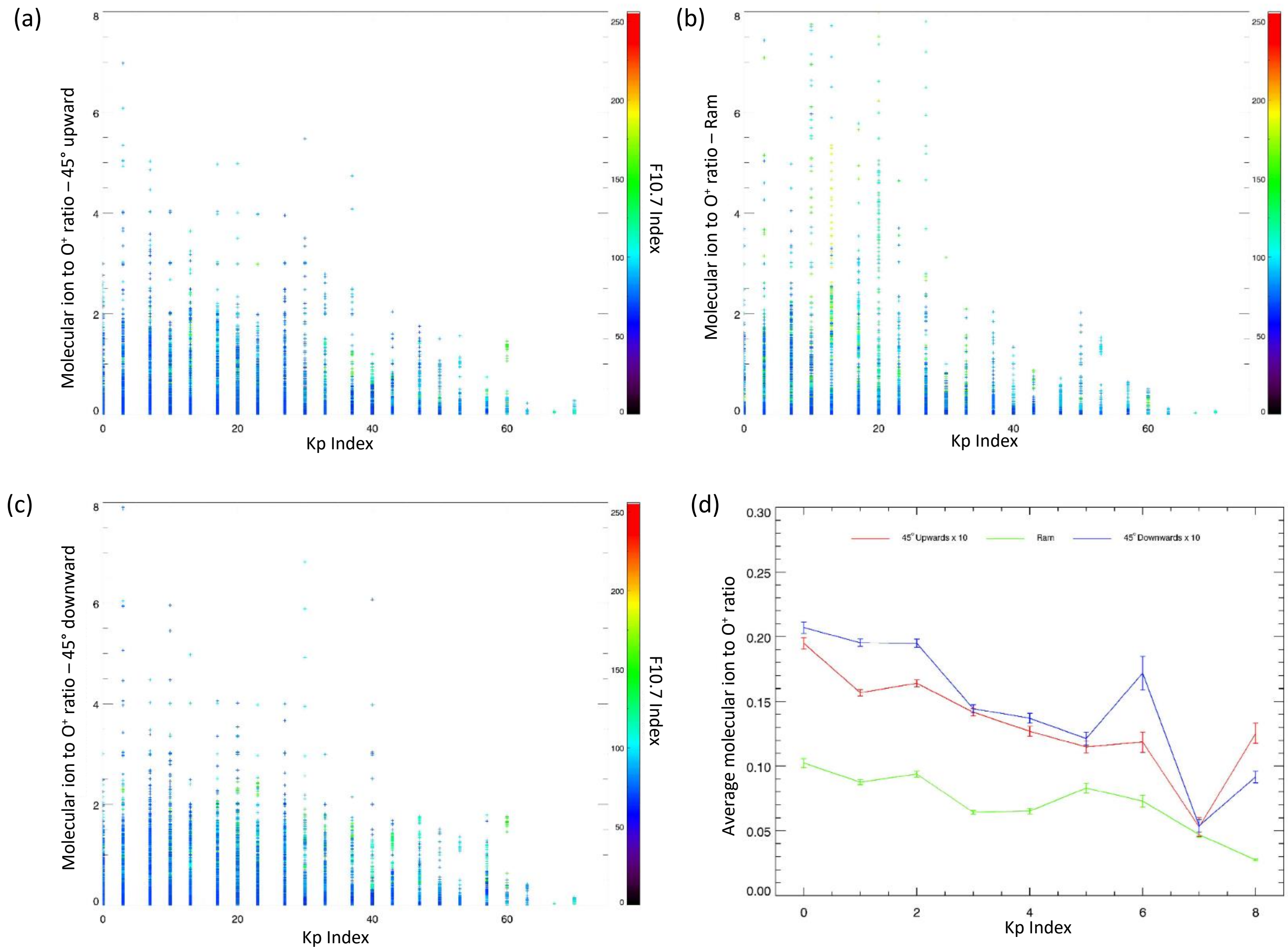

Figure 4.6: Molecular ion to O^+ ratio versus the Kp index. (a) the (45°) upward sector, (b) the ram sector, and (c) the (–45°) downward sector. (d) the average ratio in each Kp bin. The ratio seems to decrease with increasing Kp index.

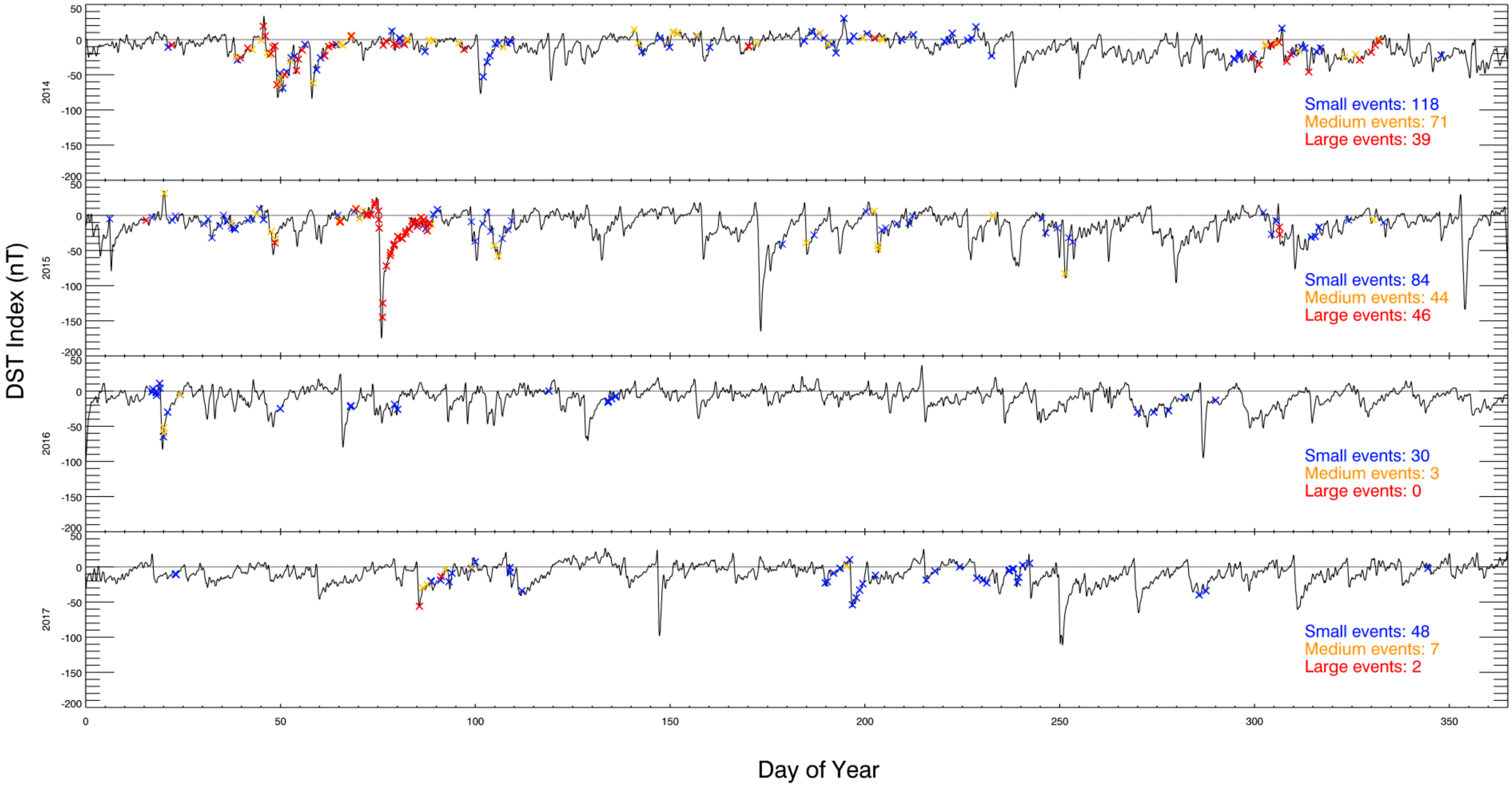

Figure 4.7: Molecular ion events compared with the Dst index. The black curve shows the time series of the Dst index from Jan 2014 to Dec 2017. Colored points denote the size of each event, with red for events with count rates exceeding 15,000 counts/s (large count rate events), orange for count rates from 10,000-15,000 counts/s (medium count rate events) and blue for count rates from 5,000-10,000 counts/s (small count rate events).

4.3 Hot Oxygen Production Simulation

The hot oxygen simulation algorithm in Chapter 3 calculates the steady-state velocity phase space density distribution $f(z)$ of atomic oxygen as a function of altitude z, by integrating the partial derivative $\partial f/\partial z$ starting at a given altitude z_0 (cf. Figure 3.11), given the altitude profiles of neutral and ion densities and temperature as model input. For our simulation we assumed a neutral temperature of 1100 K, and an electron temperature of 1600 K. These are averages for the high-latitude region of the topside ionosphere obtained from the MSISE-00 and IRI models, respectively. The hard sphere collision cross section is 1.7×10^{-15} cm^2 according to the work by Shematovich & Biskalo (1994). Integration was conducted from 200 km to 1000 km altitude, and selected results are displayed in Figure 4.8 and 4.9, with the IRI model for input O^+, O_2^+ and NO^+ ion densities.

The energy distributions of atomic oxygen in Figure 4.8 and 4.9 exhibit three distinct components, the dominant cold, ambient component (the distribution at 200 km), a component in the "transition" region, and finally the hot component at high energy. Applying a linear fitting algorithm to each component gives an effective temperature, and we expect the temperature of the hot component to correspond most closely to the inferred temperature of observed hot oxygen atoms. This temperature was estimated at various altitudes, as shown in Table 4.3, where the temperatures from the dissociative recombination of NO^+ and O_2^+ are shown separately, with the O_2^+ recombination giving a higher temperature than that of NO^+.

Table 4.2: Hot oxygen temperatures from empirical model. Hot oxygen temperatures at various altitudes from simulation using empirical models for initial density models

Altitude (km)	Hot oxygen temperature (eV) [O_2^+ recombination]	Hot oxygen temperature (eV) [NO^+ recombination]
400	0.25	0.17
600	0.25	0.17
800	0.28	0.17
1000	0.30	0.18

Figures 4.8 and 4.9 show the resulting oxygen atom energy phase space distributions from NO^+ and O_2^+ recombination, respectively, at selected altitudes. The simulation began at 200 km altitude, as noted above, so the distribution at 200 km (cyan curve) demonstrates the shape of the distribution in the absence of a hot population. Due to the larger exothermicity involved (cf. Table 2.1 in Chapter 2), the distributions from O_2^+ dissociative recombination (Figure 4.9) have a much more distinct high energy tail, and this results in a higher temperature compared with the NO^+ dissociative recombination (Figure 4.8). The atmospheric density decreases exponentially as a function of altitude, and therefore the hot oxygen atoms constitute a larger percentage of the atomic oxygen population at increasing altitude, and have an increasingly measurable fraction of the local density.

The e-POP IRM observations suggest a much higher abundance of molecular ions (molecular ion to O^+ density ratio) above 300 km than is predicted by the IRI model. Therefore, a simulation based on this model may not be a realistic description of the actual collisional relaxation dynamics. We therefore present an augmented model, wherein the IRI molecular ion concentrations are used until they reach some minimum threshold, at which point the density is set to a constant value. We chose to set a 1% and 10% minimum threshold and repeated the simulation to see their respective effect on the final hot oxygen temperature. In the case of the NO^+ recombination, the resulting distributions are presented for two selected altitudes (400 and 800 km) in Figure 4.10 and Figure 4.11, respectively. In the case of the O_2^+ recombination, the distributions resulting from these augmented density profiles are shown in Figure 4.12 and Figure 4.13, respectively. The corresponding hot oxygen temperatures are given in Table 4.3.

Table 4.3 shows that a nominal molecular ion abundance of 1% does not have much impact on the resulting temperature in either case, and that an abundance of 10% shows a more discernible departure in hot oxygen temperature from the IRI case (Table 4.2 and Figure 4.8-4.9), and most certainly from equilibrium.

It is clear that in terms of the hot atom temperature, the dissociative recombination of O_2^+ would have a greater effect on the resulting energy phase space density distribution, though observed NO^+ in the topside auroral ionosphere are much more common. The actual hot atom temperature

Table 4.3: Hot oxygen temperatures from augmented models. Hot oxygen temperatures resulting from threshold ionospheric models at various altitudes

Altitude (km)	Hot oxygen temperature [O_2^+] (eV)		Hot oxygen temperature [NO^+] (eV)	
	1%	10%	1%	10%
400	0.26	0.26	0.17	0.17
600	0.27	0.27	0.18	0.18
800	0.30	0.32	0.18	0.18
1000	0.32	0.34	0.19	0.20

likely lies somewhere in between the simulated temperatures from NO^+ and O_2^+ recombination, respectively, as some hot oxygen is produced by the dissociative recombination of each species. In the case where O_2^+ recombination dominates, one could expect a more measurable impact on the hot oxygen temperature.

Figure 4.10-4.13 show that while the effect of the augmented models on the hot oxygen *temperature* is comparatively modest relative to the IRI model, their effect on the hot to cold oxygen *density ratio* $N_{\mathrm{O,hot}}/N_{\mathrm{O,cold}}$ is much more appreciable, with an increase in $N_{\mathrm{O,hot}}/N_{\mathrm{O,cold}}$ of 1 and 2 orders of magnitude at 400 and 800 km altitude, respectively, in the case of NO^+ recombination, and a corresponding increase of a factor of ~5 and ~10 in the case of O_2^+ recombination. Figure 4.11 and Figure 4.13 show that the $N_{\mathrm{O,hot}}/N_{\mathrm{O,cold}}$ ratio is as large as ~0.1 in the high-altitude topside ionosphere in the case of the augmented models.

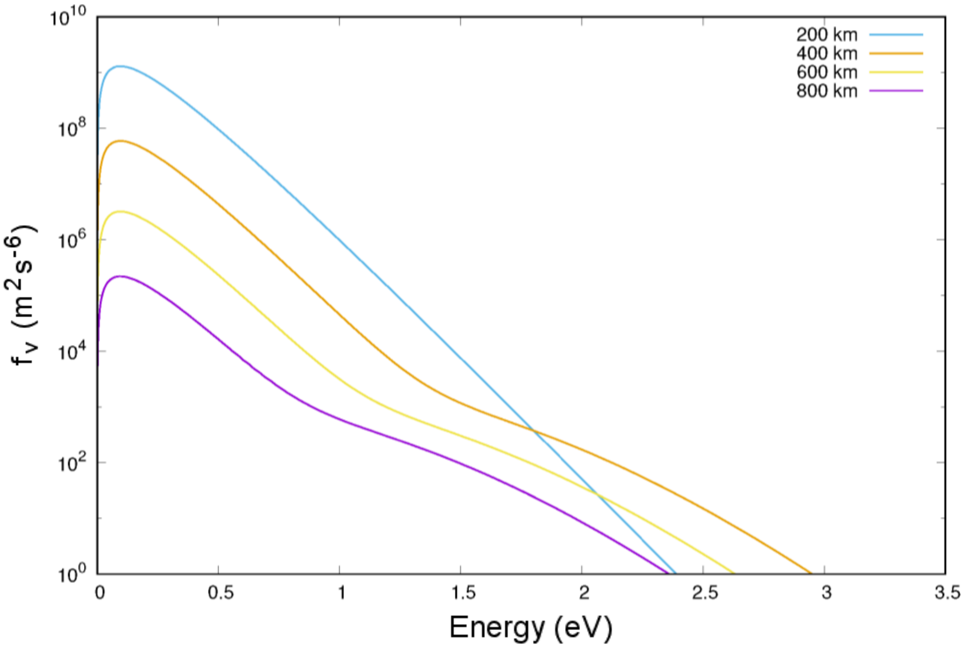

Figure 4.8: Phase space distributions of atomic oxygen from NO^+ recombination – IRI model. The energy phase space distribution of hot oxygen atoms resulting from the dissociative recombination of NO^+ is shown at various altitudes. The blue curve is for the starting altitude of 200 km in our simulation, and shows the distribution in the absence of the hot atoms.

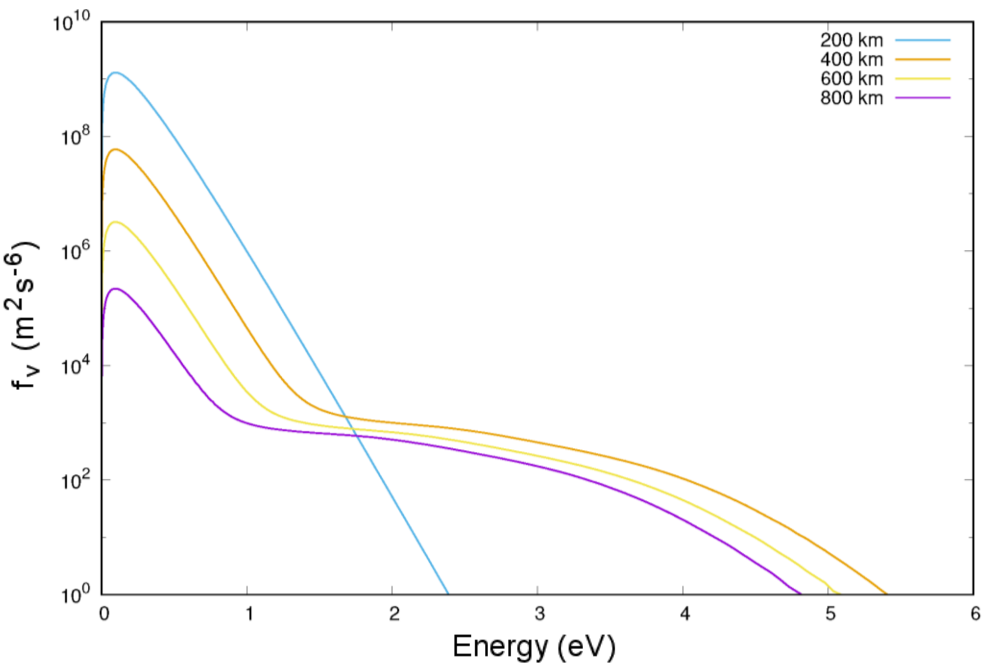

Figure 4.9: Phase space distributions of atomic oxygen from O_2^+ Recombination – IRI Model. The energy phase space distribution of hot oxygen atoms resulting from the dissociative recombination of O_2^+ is shown at various altitudes. The distributions above the starting altitude of 200 km have a pronounced high energy tail, compared with the cold atom distribution at 200 km, (blue curve).

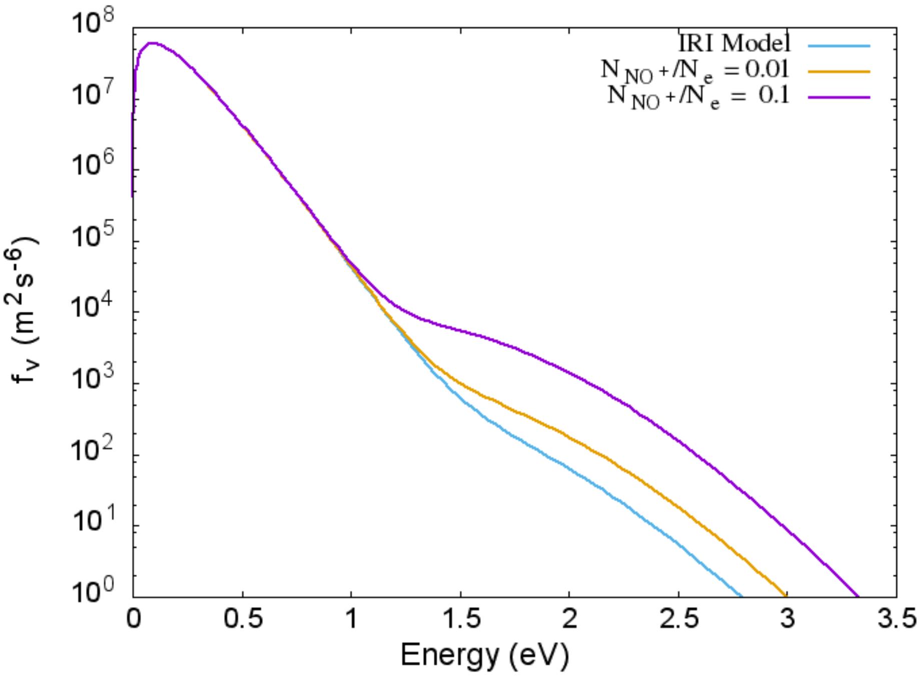

Figure 4.10: Comparison of oxygen atom energy phase space distributions from NO^+ recombination – 400 km. A comparison of the simulation results using the IRI model and threshold NO^+ density models, respectively, of hot atomic oxygen production due to the dissociative recombination of NO^+ at 400 km altitude: Minimum NO^+ densities of 1% and 10% are shown.

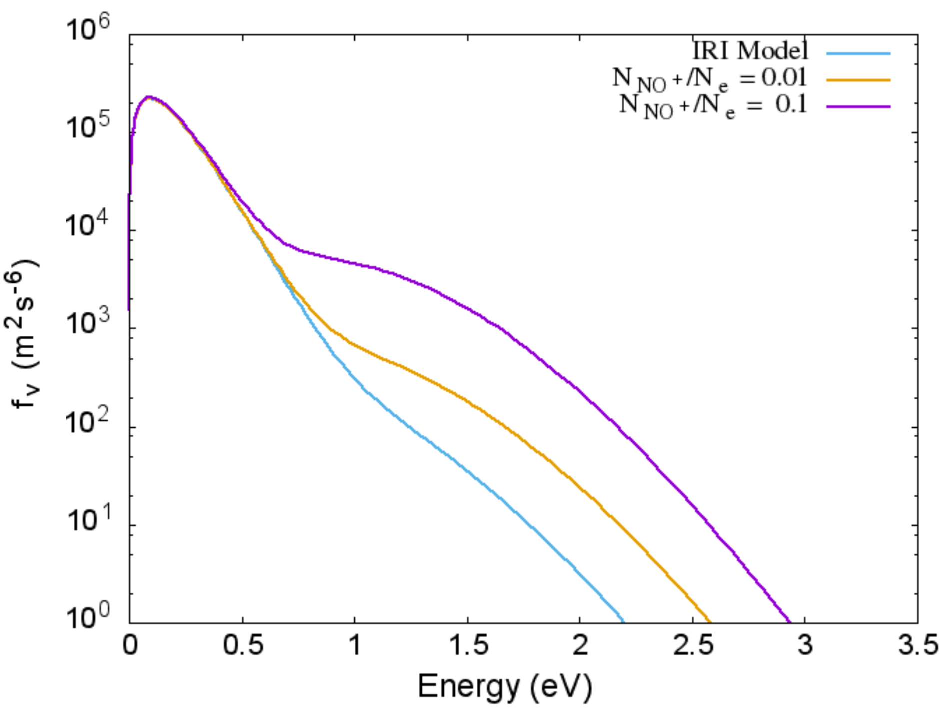

Figure 4.11: Comparison of oxygen atom energy phase space distributions from NO^+ recombination – 800 km. A comparison of the simulation results using the IRI model and threshold NO^+ density models, respectively, of hot atomic oxygen production due to the dissociative recombination of NO^+ at 800 km altitude: Minimum NO^+ densities of 1% and 10% are shown.

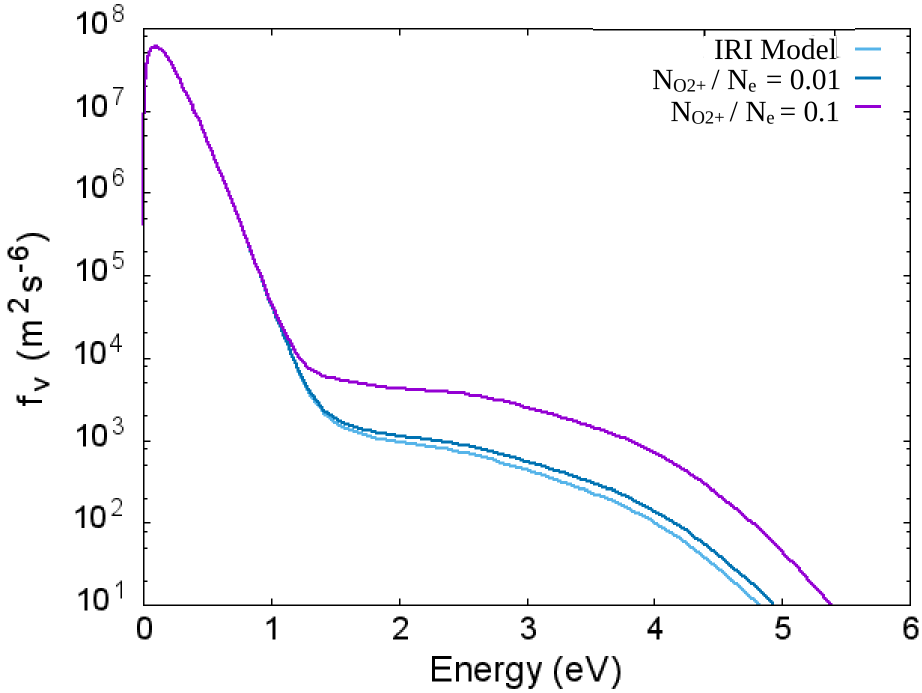

Figure 4.12: Comparison of oxygen atom energy phase space distributions from O_2^+ recombination – 400 km. A comparison of the simulation results using the IRI model and threshold O_2^+ density models, respectively, of hot atomic oxygen production due to the dissociative recombination of O_2^+ at 400 km altitude: Minimum O_2^+ densities of 1% and 10% are shown.

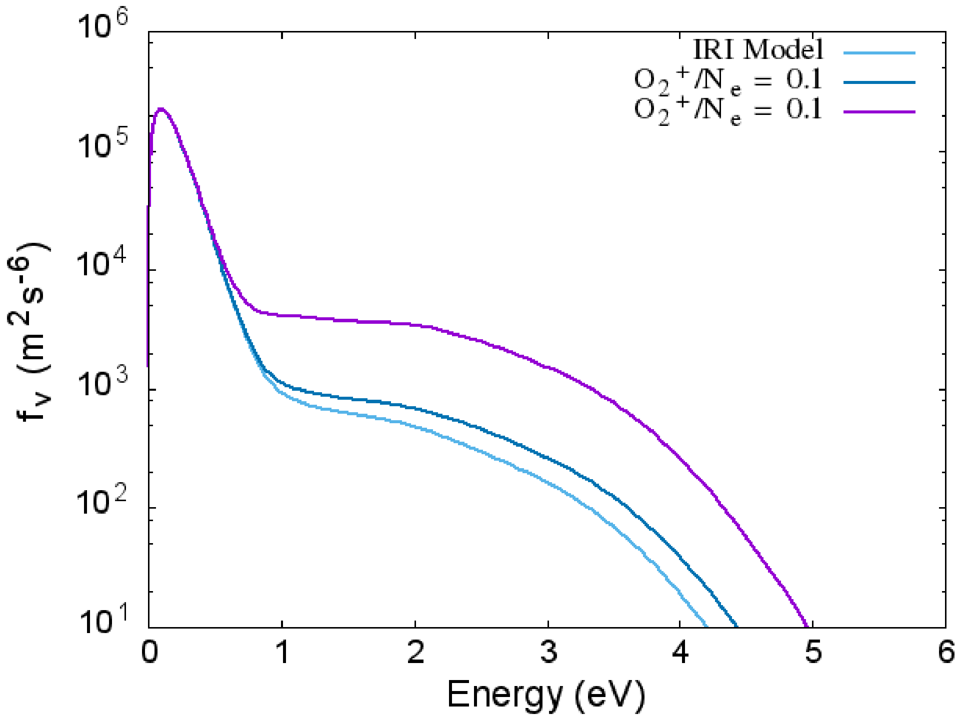

Figure 4.13: Comparison of oxygen atom energy phase space distributions from O_2^+ recombination – 800 km – A comparison of the simulation results using the IRI model and threshold O_2^+ density models, respectively, of hot oxygen production due to the dissociative recombination of O_2^+ at 800 km altitude: Minimum O_2^+ densities of 1% and 10% are shown.

5 Discussion and Conclusions

In this final chapter we discuss the scientific significance of the results in Chapter 4, and their implications on magnetosphere-ionosphere-thermosphere coupling and on the future directions of our research.

5.1 Molecular Ion Occurrence Morphology

Molecular ions have previously been observed in the upper atmosphere and magnetosphere, though these instances are relatively rare. We have presented evidence that molecular ions occur frequently at all e-POP altitudes, from 325 to 1500 km. The abundance and geospatial locations of these events vary, though large count rate events peak in the pre-midnight sector, and small count rate events in the 8-10 MLT range.

It has been demonstrated that energetic plasma injection events during low to moderate solar activity primarily occur in the pre-midnight sector, within 2 h of 23 MLT (Beharrell et al., 2015). Night-side precipitating energetic electrons can penetrate deeper into the ionosphere compared with their less energetic daytime counterparts, so it is quite possible that these night-side energetic precipitation events are more effective in producing ionization in the lower-altitude region, where the molecular N_2 and O_2 densities are higher, leading to these large count rate events involving higher molecular ion concentrations. Conversely, on the day side we see a higher percentage of small count rate events. It is likely that the precipitation of less energetic electrons, which do not penetrate as deep into the ionosphere, produce events with smaller count rates and involve smaller concentrations of molecular ions.

The large count rate events appear to be associated with the large magnetic storms; Figure 4.7(a-2015) is a good example of this. There is one clearly discernible storm, which occurred in March

2015, and is the largest of our entire data set. The storm contains many large molecular ion events, more than any other storm. Forty out of the 46 large molecular ion count rate events in 2015 occurred in the onset and recovery phases of this storm.

This storm is considered a 'superstorm,' and it was caused by a large coronal mass ejection (CME) and has been the subject of many studies. A severe ionospheric density depletion was reported at high-latitudes, as well as other ionospheric disturbances (Cherniak, Zakharenkova, & Redmon, 2015).

It is important to note that our data set covers only a small percentage (<10%) of storm time events, due to the low operation duty cycle of the e-POP satellite. Moreover, our data set likely under samples or even misses the regions of peak ion-flux during very active times (large AE) and large magnetic storms. In cases of large magnetic storms, it is well documented that the auroral oval moves equatorward. As e-POP concentrates its data collection at high latitudes (generally above 45°-50°), it is possible that IRM may sometime fail to sample the peak or "most interesting" region of a storm-time or disturbed-time event.

Our study demonstrates the presence of molecular ions in ion upflows, as they have been frequently detected in the 45°, upward pixel sectors. It is important to note that (*i*) the spacecraft ram velocity is about 7-8 km/s and primarily in the horizontal direction, (*ii*) the observed count rate in the upward (downward) detector pixel sector is small but nevertheless non-negligible compared with that in the ram sector, and that (*iii*) the detector pixels have a finite angle of acceptance (7.4°–28.0° for detector-pixel 3-6, where the ion count-rate is typically the highest; Yau et al., 2018). Taken together, this implies that in the ionosphere frame of reference, the upward (downward) ion velocity of the observed ions in the 45° (–45°) detector sector is comparable to the thermal speed (~1 km/s for NO^+ at an ion temperature of 0.1 eV) and small compared with the spacecraft velocity.

Figure 4.3(d) further demonstrates that the upward and downward fluxes of molecular ions are approximately equal, though the upward ion fluxes are slightly higher. A small fraction of the ions is likely accelerated further above the F region to high enough escape velocities, and these ions do not return to the topside ionosphere, as discussed in Yau & Andre (1997). However, the majority of the ions do not attain enough energy to overcome gravitation and therefore eventually return to the ionosphere, and appear as downward moving ions.

5.2 Hot Oxygen Simulations

The dissociative recombination and subsequent collisional relaxation of molecular NO^+ and O_2^+ ions produce hot oxygen atoms, which contribute to the heating of the upper atmosphere. We presented simulation results using the IRI model, which suggest a hot oxygen temperature of ~0.17 eV, and ~0.25 eV in the case of NO^+ and O_2^+ dissociative recombination, respectively. These results are likely lower-limit estimates, and the simulated hot to cold oxygen densities are likely to be significant underestimates, since the IRI model significantly underestimates the F-region densities of molecular ions at high latitudes.

Using an augmented density profile based on the IRM observations, the effects of molecular ion concentrations of 1 and 10 percent above 300 km altitude were assessed. This yielded hot oxygen temperatures of 0.18 and 0.19 eV, respectively in the case of NO^+, and 0.28 and 0.3 eV in the case of O_2^+. Depending on the observation technique used, the predicted temperature difference and density ratio between the cold and hot oxygen atoms could possibly be detected with in situ or remote-sensing optical measurements.

The work by Yee (1988) suggested a hot oxygen temperature of ~0.4 eV above 550 km, a result which was later supported by the work of Hedin (1989). However, both measurements are believed to be subject to large uncertainties. While our simulated O_2^+ temperature alone is in agreement with these results, the apparent agreement may well be fortuitous. It is possible that the NO^+ recombination constitutes the dominant source of hot oxygen in the high-latitude topside ionosphere, with the resulting hot temperature in the range between ~0.2 and 0.3 eV.

5.3 Conclusions

We live in a society highly dependent on space-based communication and navigation. Communication and navigation satellites propagate their signals through the ionosphere, where small-scale plasma density structures (density irregularities) can act like bubbles in a lens, distorting the signals. Additionally, structures or localized regions of enhanced mass density provide an additional amount of drag on LEO spacecraft, leading to anomalous orbit decay. A better understanding of atmospheric dynamics, MIT coupling in particular, improves our ability to predict space weather, and our ability to forecast its impacts on both terrestrial and space-based technological infrastructure and systems and to mitigate these impacts on our increasingly technology-dependent society.

In this work we have presented two distinct, but related, results which contribute to our understanding of ionospheric dynamics and MIT coupling. The first result relates to the occurrence morphology of molecular ions in the topside ionosphere at high latitudes. These ions are present at much higher altitudes than current models predict, and in much greater abundances than predicted. We measured molecular ions at all e-POP altitudes, during both active and quiet geomagnetic times.

Large count rate molecular ion events occur in greater frequency in the pre-midnight (20-22 MLT) sector, which coincides with the peak region for energetic precipitating electrons. These large count rate events also seem to show a correlation to large geomagnetic storms, with most occurring in the main and recovery phases.

We have shown that the presence of molecular ions in the high-latitude, auroral ionosphere could have a measurable impact on the mass density and composition in the topside thermosphere as these ions undergo dissociative recombination to form non-thermal (or “hot”) atomic oxygen. Augmented molecular ion composition ratios of 10 percent were modeled, giving a resulting hot oxygen temperature of 0.18 eV and 0.30 eV, for NO^+ and O_2^+, respectively at 600 km.

5.4 Future Directions of Research

With an initial survey of the occurrence morphology and frequency of molecular ions complete, the next useful task would be to develop a method to discern each species from the others. This is important in the case of distinguishing N^+ from O^+, and separating N_2^+, NO^+, and O_2^+ as unique molecular species. This will help shed light on the relation between particular molecular species and the N^+ enhancement that has been noted in this study as well as others. Furthermore, once all the ion species can be separated from one another it will be possible to estimate the absolute density of molecular ions in the topside ionosphere.

Most of the data used for this investigation were collected near solar minimum. A further investigation is required to determine if or how the occurrence morphology, occurrence frequency, and therefore the resulting hot atomic oxygen population, change as a function of solar activity. e-POP has recently received funding to extend its mission operation, meaning we will have the opportunity to obtain four more years' worth of data as we exit solar minimum.

A direct measurement of the hot oxygen geocorona would be scientifically significant, though atmospheric neutrals are notoriously difficult to measure. e-POP has a neutral mass spectrometer (NMS) on board, but the analysis and interpretation of the data from NMS have proven to be challenging to date, and hence the NMS data have not been not included in this study. However, effort to better understand and interpret the NMS measurements is ongoing. There are also future missions which will bear on this scientific question.

The Global-scale Observations of the Limb and Disk (GOLD) spacecraft was launched in January 2018 and it is set to study the effect of geomagnetic storms on the temperature and composition structure of the upper atmosphere. Residing in geostationary orbit, this spacecraft uses a high resolution far-ultraviolet imaging spectrograph to scan the limb and disk of Earth every 30 minutes, which will provide high-quality limb scans of atomic oxygen and other atmospheric emissions.

The Ionospheric Connection Explorer (ICON) mission, whose launch was recently delayed, has been designed to study the boundary between the ionosphere, thermosphere and magnetosphere. It aims to measure the impact of "space weather" on atmospheric variations. The anticipated observations from ICON will likely shed further light on the topic of hot oxygen also.

References

Bartels, J., Heck, N. H., & Johnston, H. F. (1939). The three-hour-range index measuring geomagnetic activity. *Terrestrial Magnetism and Atmospheric Electricity, 4*(411-454), 44.

Beharrell, M. J., Honary, F., Rodger, C. J., & Clilverd, M. A. (2015). Substorm-induced energetic electron precipitation: Morphology and prediction. *Journal of Geophysical Research*, 2993-3008.

Bilitza, D. (2001). International Reference Ionosphere 2000. *Radio Science*, *36*(2), 261-275

Bilitza, D., & Reinisch, B. W. (2008). International Reference Ionosphere 2007: Improvements and new parameters. *Advances in Space Research, 42*, 599-609, doi:10.1016/j.asr.2007.07.048.

Bisikalo, D. V., Shematovich, V. I., & Gerard, J. C. (1995). A kinetic model of the formation of the hot oxygen geocorona 2. Influence of O^+ ion precipitation. *Journal of Geophysical Research, 100*(A3), 3715-3720.

Cherniak, I., Zakharenkova, I., & Redmon, R. J. (2015). Dynamics of the high-latitude ionospheric irregularities during the 17 March 2015 St. Patrick's Day storm: Ground-based GPS measurements. *Space Weather*, 585-597.

Cotton, D. M., Gladstone, G. R., & Chakrabarti, S. (1993). Sounding rocket observation of a hot atomic oxygen geocorona. *Journal of Geophysical Research, 98*(A12), 21651-21657.

Craven, P., Chappell, C., Kakani, L., & Olsen, R. (1985). Observations of molecular ions in the earth's magnetosphere. *Journal of Geophysical Research, 90*, 7599-7605.

Hedin, A. E. (1989). Hot oxygen geocorona as inferred from neutral exospheric models and mass spectrometer measurements. *Journal of Geophysical Research, 94*(A5), 5523-5529.

Hernandez, G. (1971). The signature profiles of O(1S) in the airglow. *Planetary Space Science, 19*, 467-476.

Hickey, M. P., Richards, P. G., & Torr, D. G. (1995). New sources for the hot oxygen geocorona: Solar cycle, seasonal, latitudinal, and diurnal variations. *Journal of Geophysical Research, 100*(A9), 17377-17388.

Hoare, M. R., & Kaplinsky, C. H. (1970). Linear hard-sphere gas: Variational eigenvalue spectra of the energy kernel. *Journal of Chemical Physics, 52*(7), 3336-3353.

Hodges Jr., R. R. (2000). Distributions of hot oxygen for Venus and Mars. *Journal of Geophysical Research, 105*(E3), 5971-6981.

Hoffman, J. H., Dodson, W. H., Lippincott, C. R., & Hammack, H. D. (1974). Initial ion composition results from the Isis 2 satellite. *Journal of Geophysical Research, 79*(28), 4246-4251.

Kabin, K., & Shizgal, B. D. (2002). Velocity distributions of energetic atoms in planetary exospheres from dissociative recombination. *Journal of Geophysical Research, 107*(E7), 71-79.

Kella, D., Sogaard, L. V., Jonhson, P. J., Pedersen, H., & Andersen, L. H. (1997). The source of green light emission determined from a heavy-ion storage ring experiement. *Science, 276*, 1530-1533.

Klecker, B., Mobius, E., Hovestadt, D., Scholer, M., Gloeckler, G., & Ipavich, F. M. (1986). Discovery of energetic molecular ions (NO^+ and O_2^+) in the storm time ring current. *Geophysical Research Letters, 13*(7), 632-635.

Massey, H. S. (1937). Dissociation, recombination and attachment processes in the upper atmosphere. *Proceedings of the Royal Society of London*, *169*(915), 542-553.

Meriwether, J. W., Biondi, M. A., & Anderson, D. N. (1985). Equatorial airglow depletions induced by thermospheric winds. *Journal of Geophysical Research*, 12(8), 487-490.

Peterson, W. K., Abe, T., Fukunishi, H., Greffen, M.J., Hayakawa, H., Kasahara, Y., Kimura, I., Matsuoka, A. (1994). On the sources of energization of molecular ions at ionospheric altitudes. *Journal of Geophysical Research, 99*(A12) 23,257-23,274.

Picone, J. M., Hedin, A. E., Drob, D. P., & Aikin, A. C. (2002). NRLMSIS-E00 empirical model of the atmosphere: Statistical comparisons and scientific issues. *Journal of Geophysical Research, 107*(A12),1468, doi:10.1029/2002JA009430.

Richards, P. G., Hickey, M. P., & Torr, D. G. (1994). New sources for the hot oxygen geocorona. *Geophysical Research Letters, 21*(8), 657-660.

Roble, R. G., Ridley, E. C., Richmond, A. D., & Dickinson, R. E. (1988). A coupled thermosphere/ionosphere general circulation model. *Geophysical Research Letters, 15*(12), 1325-1328, doi:10.1029/GL015i012p01325.

Rohrbaugh, R. P., & Nisbet, J. S. (1973). Effect of energetic oxygen atoms on neutral density models. *Journal of Geophysical Research, 78*(28), 6768-6772.

Rostoker, G. (1972). Geomagnetic indices. *Reviews of Geophysics and Space Physics, 10*(4), 935-950.

Saroso, S., Iyemori, T., and Sugiura, M. (1993). Universal time variations in the ap and Dst indices and their possible cause, *Journal of Geomagnetism and Geoelectricity, 45*(7), 563-572.

Schunk, R., & Nagy, A.F. (2009). *Ionopheres: Physics, Plasma Physics, and Chemistry.* Cambridge, UK: Cambridge University Press.

Sheehan, C. H., & St. Maurice, J. P. (2004). Dissociative recombination of N_2^+, O_2^+, and NO^+: Rate coefficients for ground state and vibrationally excited ions. *Journal of Geophysical Research, 109*, 1-21.

Shematovich, V. I., & Bisikalo, D. V. (1994). A kinetic model of the formation of the hot oxygen geocorona 1. Quiet geomagnetic conditions. *Journal of Geophysical Research, 99*(A12), 23217-23228.

Shematovich, V. I., & Bisikalo, D. V. (2005). An auroral source of hot oxygen in the geocorona. *Geophysical Research Letters,* L02105, doi:10.1029/2004GL021912.

Shematovich, V. I., Bisikalo, D. V., Krauss, S., Hausleitner, W., & Lammer, H. (2011). Influence of the hot oxygen corona on the satellite drag in the earth's upper atmosphere. *Solar System. Research, 45*(3), 231-239.

Tapping, K. F. (2013). The 10.7 cm solar radio flux (F10.7). *Space Weather, 11*, 394-406.

Taylor, Jr., H. (1974). High latitude minor enhancements: a clue for studies of magnetosphere-atmosphere coupling. *Journal of Atmospheric and Terrestrial Physics*, *36*, 1815-1823.

Vejby-Christensen, L., Kella, D., Pedersen, H. B., & Andersen, L. H. (1998). Dissociative recombination of NO^+. *Physical Review A, 57*, 3627-3634.

Whipple, E. C. (1974). Theory of reaction product velocity distributions. *Journal of Chemical Physics, 60*(4), 1345-1351.

Yau, A. W., & Andre, M. (1997). Source processes in the high latitude ionosphere. *Space Science Review*, *80*, 1-25

Yau, A. W., & Howarth, A. (2016). Imaging thermal plasma mass and velocity analyzer. *Journal of Geophysical Research*, *121*, 7326-7333.

Yau, A. W., & James, H. G. (2015). CASSIOPE Enhanced Polar Outflow Probe (e-POP) mission overview. *Space Science Reviews, 189*(1-4), 3-14.

Yau, A. W., Foss, V., Howarth, A. D., Perry, G. W., Watson, C., & Huba, J. (2018). Eclipse-induced changes to the topside ion composition and field-aligned flows in the August 2017 solar eclipse: e-POP observations. *Geophysical Research Letters*, *45*, 10,829–10,837. https://doi.org/10.1029/2018GL079269.

Yau, A. W., Peterson, W. K., & Abe, T. (2011). Influences of the ionosphere, thermosphere and magnetosphere on ion outflows. In *The Dynamic Magnetosphere* (pp. 283-314). Netherlands: Springer Science+Business Media.

Yau, A. W., Whalen, B. A., Goodenough, C., Sagawa, E., & Mukai, T. (1993). EXOS D (Akebono) observations of molecular NO^+ and N_2^+ upflowing ions in the high-altitude auroral ionosphere. *Journal of Geophysical Research, 98*(A7), 98, 11205-11224.

Yee, J. H., Meriwether, J. W., & Hays, P. B. (1980). Detection of a corona of fast oxygen atoms during solar maximum. *Journal of Geophysical Research, 85*(A7), 3396-3400.

Yee, J. H. (1988). Non-thermal distribution of O(1D) atoms in the night-time thermosphere. *Planetary and Space Science, 36*(1), 89-97.